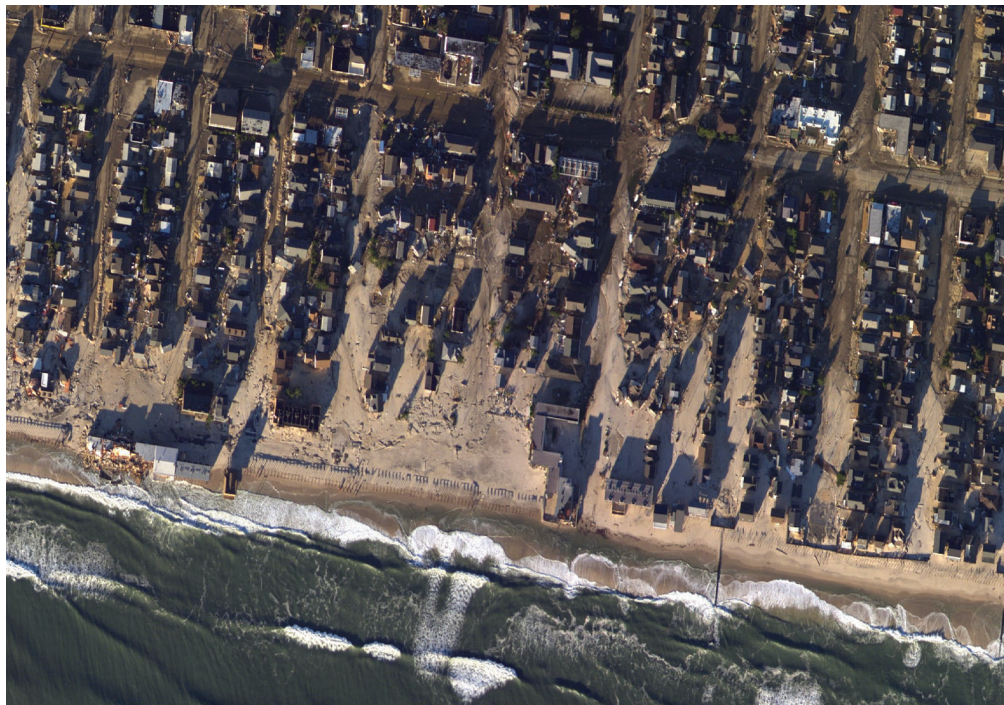


Coastal Inundation in Developed Regions: Experimental Results and Implications for Engineering Practice



Applied Technology Council

Prepared for
University of Notre Dame

Funded by
National Institute of Standards and Technology

Applied Technology Council

The Applied Technology Council (ATC) is an internationally recognized non-profit corporation founded by the Structural Engineers Association of California in 1973 to protect life and property through the advancement of science and engineering technologies. With a focus on seismic engineering, and demonstrated capabilities in wind, coastal inundation, and blast engineering, ATC develops state-of-the-art, user-friendly engineering resources and applications to mitigate the effects of natural and other hazards on the built environment. ATC implements funded research and technology transfer projects through the development of nonproprietary consensus opinions on structural engineering issues. ATC also identifies and encourages needed research, and disseminates technological advancements through guidelines, manuals, seminars, workshops, forums, and electronic media.

ATC consists of a small group of in-house technical and support staff, assisted by highly qualified individuals engaged as consultants or subcontractors on specific projects. With this model, ATC is able to assemble teams of researchers and practitioners in diverse areas of expertise that would not otherwise be available through any one organization. Funding for ATC projects comes from federal, state, and local government entities, or from the private sector in the form of tax-deductible contributions to the ATC Endowment Fund.

ATC is guided by a nationally recognized Board of Directors consisting of representatives appointed by the American Society of Civil Engineers, the National Council of Structural Engineers Associations, the Structural Engineers Association of California, the Structural Engineers Association of New York, and five at-large members representing different areas of engineering practice. Each director serves a three-year term.

2022 Board of Directors

Ryan A. Kersting, President

David O. Prevatt, Vice President

Michael L. Cochran, Secretary/Treasurer

Donald O. Dusenberry, Past President

Melissa Burton

Lyle P. Carden

Kelly Cobeen

Maria E. Garlock

Carrie J. Johnson

Christopher W. Letchford

Ahmad Rahimian

Jose Restrepo

Seth Thomas

Christos Tokas

ATC Disclaimer

Although the information presented in this publication is believed to be correct, ATC makes no warranty, expressed or implied, and assumes no responsibility for the accuracy or completeness of the information or opinions expressed herein. The material presented in this publication should not be used or relied upon without competent examination by qualified professionals or without verification of the accuracy or suitability for the intended application. Users of information from this publication assume all liability arising from such use.

Cover image: New Jersey Coast after Hurricane Sandy in 2012 (photo credit: NOAA).

ATC-149

Coastal Inundation in Developed Regions: Experimental Results and Implications for Engineering Practice

Prepared by
APPLIED TECHNOLOGY COUNCIL
201 Redwood Shores Parkway, Suite 240
Redwood City, California 94065
www.ATCouncil.org

Prepared for
UNIVERSITY OF NOTRE DAME
Andrew Kennedy, Principal Investigator
Notre Dame, Indiana

and
NATIONAL INSTITUTE OF STANDARDS AND TECHNOLOGY
Gaithersburg, Maryland

APPLIED TECHNOLOGY COUNCIL
Jon A. Heintz (Project Manager)

PROJECT OVERSIGHT COMMITTEE
Christopher P. Jones (Project Technical Director)
A. Christopher Cerino
Robert A. Dalrymple
Seth Thomas

WORKING GROUP MEMBERS
Joaquin P. Moris

2022

Preface

In 2017, the University of Notre Dame entered into a cooperative agreement (70NANB17H278) with the National Institute of Standards and Technology (NIST) entitled “Coastal Inundation Events in Developed Regions.” The purpose of this agreement was to conduct a multi-year research effort to develop and test methodologies to improve predictions of inundation hydrodynamics and loading in developed (urban) regions for both storm wave and tsunami inundation. In 2018, the Applied Technology Council (ATC) received a subaward (203181ATC) from the University of Notre Dame to form a Project Oversight Committee to review and advise on the research plan, and to assist in the translation of results into engineering practice.

Improved information on how waves, currents, and floodborne debris propagate through the built environment in coastal inundation events is needed because computations using bare-earth assumptions are widely believed to introduce errors in estimates of hydrodynamic conditions and structural load calculations. Moreover, simplified approaches to design are often very conservative, especially when a building is situated within an array of buildings.

Laboratory and numerical experiments considered wave and current flow through a rectangular array of rigid buildings with a consistent size and spacing. Waves and currents were perpendicular to the shoreline and the rows of buildings in the array, and the landward boundary of the array drained into a channel, allowing a net flow of fluid through the array. The propagation of waves, currents, and floodborne debris throughout the array were observed and measured, and the results used to develop recommended improvements or enhancements to present design practice and potential changes to flood design provisions in future building codes and standards.

ATC is indebted to the leadership of Andrew Kennedy as Principal Investigator for this work, and Joaquin Moris for the conduct of laboratory and numerical experiments. ATC is also indebted to the members of the Project Oversight Committee, including Chris Jones (Project Technical Director), Chris Cerino, Tony Dalrymple, and Seth Thomas, for their efforts

in reviewing and extrapolating results in the development of recommendations for practical use.

ATC gratefully acknowledges the funding provided by the University of Notre Dame and the National Institute of Standards and Technology, and gratefully recognizes Bernadette Hadnagy and Ginevra Rojahn for ATC report production support.

Jon A. Heintz
ATC Executive Director

Table of Contents

| | |
|--|------------|
| Preface..... | iii |
| List of Figures..... | vii |
| List of Tables | xi |
| 1. Introduction..... | 1-1 |
| 1.1 Problem Statement and Motivation | 1-1 |
| 1.2 Project Overview and Approach | 1-3 |
| 1.3 Description of Present Design Practice | 1-3 |
| 1.4 Resources for Present Design Practice and their Limitations... | 1-4 |
| 1.4.1 Flood Hazard Maps and Studies..... | 1-5 |
| 1.4.2 Local or State Floodplain Management Regulations .. | 1-5 |
| 1.4.3 Building Codes and Standards | 1-5 |
| 1.5 Report Organization and Content..... | 1-6 |
| 2. Overview of Research and Experimental Results | 2-1 |
| 2.1 Experimental Set-Up | 2-1 |
| 2.2 Wave Runup within an Array..... | 2-3 |
| 2.3 Wave Loads within an Array..... | 2-4 |
| 2.4 Debris Impact within an Array | 2-7 |
| 3. Implications and Limitations of Experimental Results | 3-1 |
| 3.1 Wave Transmission | 3-1 |
| 3.2 Wave Load Effects Due to Row Spacing, Distance from Shoreline, and Lateral Building Offsets | 3-5 |
| 3.2.1 Alongshore Spacing of Buildings..... | 3-6 |
| 3.2.2 Cross-Shore Spacing of Buildings | 3-7 |
| 3.2.3 Distance from the Shoreline | 3-9 |
| 3.2.4 Lateral Building Offsets | 3-9 |
| 3.3 Reflected Waves..... | 3-10 |
| 3.4 Maximum Inundation Levels, Cross-Shore Velocity, and Cross-Shore Momentum Flux | 3-11 |
| 3.4.1 Wave Conditions | 3-11 |
| 3.4.2 Current-Only Conditions | 3-12 |
| 3.4.3 Effect of Boundary Conditions at the Landward End of a Building Array | 3-13 |
| 3.5 Probability of Debris Impact within an Array | 3-14 |
| 3.6 Variation of Debris Impulse within an Array | 3-15 |
| 3.7 Maximum Loads from Debris | 3-18 |
| 3.7.1 SDOF Model and Modifications | 3-18 |
| 3.7.2 Comparison of ASCE 7-22 Flood and Tsunami Loads | 3-20 |

| | | |
|---|---|------------|
| 4. | Recommendations..... | 4-1 |
| 4.1 | Improvements to Present Design Practice | 4-1 |
| 4.2 | Flow Depths and Velocities..... | 4-2 |
| 4.3 | Wave Loads | 4-3 |
| 4.3.1 | Variation of Wave Loads within an Array..... | 4-4 |
| 4.3.2 | Wave Load Reduction Factors..... | 4-4 |
| 4.3.3 | Reflected Waves | 4-5 |
| 4.4 | Debris Impact in Wave and Current Conditions..... | 4-5 |
| 4.4.1 | Likelihood of Debris Impact..... | 4-6 |
| 4.4.2 | Debris Impact Loads..... | 4-8 |
| 4.5 | Recommendations for Further Study..... | 4-9 |
| Appendix A: National Academy of Sciences Formula | | A-1 |
| Symbols | | B-1 |
| References | | C-1 |
| Project Participants..... | | D-1 |
| Applied Technology Council Directors | | E-1 |

List of Figures

| | | |
|--------------|--|-----|
| Figure 1.1-1 | Plan view showing simplified building array and definitions of key terms | 1-2 |
| Figure 2.1-1 | Experimental set-up: (A) isometric representation of the DWB; (B) cross-shore elevation view in the center of the DWB; (C) plan view of the concrete beach, including the location of the video cameras; and (D) location of instrumentation in the test section..... | 2-2 |
| Figure 2.3-1 | Example of laboratory and computational loading for rows 1-5 | 2-5 |
| Figure 2.3-2 | Illustration of important load quantities in three cases: (a) bare earth simulation with all structures removed for maximum momentum flux, velocity, and surface elevation; (b) unobstructed load on a structure in an array with n sheltering rows removed; and (c) sheltered load case with n sheltering rows in place | 2-5 |
| Figure 2.3-3 | Numerical and experimental Load Reduction Factors $LRFA_n$, $LRFB_n$, and $LRFC_n$ as a function of the number of rows providing shelter, n | 2-6 |
| Figure 3.1-1 | NAS transmission coefficient, B , as a function of the number of seaward rows of buildings, n , and gap ratio, r | 3-2 |
| Figure 3.1-2 | Load Reduction Factor (LRF) derived from the NAS transmission coefficient (solid line), as a function of the number of rows of buildings providing shelter, n , plotted along with experimental data ($r = 0.6$)..... | 3-4 |
| Figure 3.1-3 | Load Reduction Factor (LRF) derived from the NAS transmission coefficient, as a function of the number of seaward rows of buildings, n , and gap ratio, r | 3-5 |
| Figure 3.2-1 | Comparison of laboratory video and numerical modeling results | 3-6 |
| Figure 3.2-2 | Plot of $LRFA$ versus blockage ratio, w^* , showing the effect of building spacing on wave loads in row 2; numerical results from Moris et al. (2021) shown in blue for two different tsunami waves (symbols o and \times), and NAS load reductions shown in red (symbol \times)..... | 3-7 |

| | | |
|--------------|--|------|
| Figure 3.2-3 | Tsunami water surface elevations around two coastal structures | 3-8 |
| Figure 3.2-4 | Plot of $LRFA$ versus nondimensional distance between rows, d^* , showing the effect of row spacing on wave loads in row 2, for $w^* = 0.4$ | 3-8 |
| Figure 3.2-5 | Ratio of Load Reduction Factors, $LRFB_n$ and $LRFA_n$ as a function of the number of rows of buildings providing shelter, showing the effect of distance from the shoreline | 3-9 |
| Figure 3.2-6 | Plot of $LRFA$ versus nondimensional offset, o^* , showing the effect of building offset on wave loads in row 2 | 3-10 |
| Figure 3.4-1 | Numerical run-up reduction factors, RRF , velocity reduction factors, VRF , and momentum flux reduction factors, MRF , as a function of the number of rows providing shelter, n | 3-11 |
| Figure 3.4-2 | Mean velocities from current-only experimental tests, measured in the centerline of cross-shore streets (open circles), compared with the velocity just outside the array multiplied by $1/r = 1/0.6$ (dashed line)..... | 3-13 |
| Figure 3.4-3 | Computed stillwater surface elevations along the centerline of cross-shore streets (solid line), showing values 0.1m in front of Rows 1-6 (red dots); colors indicate instantaneous velocities for current-only flow..... | 3-13 |
| Figure 3.5-1 | Results from debris impact experiments: (A) collision map showing the total number of collision events in each building for the wave-current condition, $N_T = 1170$; (B) collision map showing the total number of collision events in each building for the current-only condition, $N_T = 156$; and (C) collision ratio as a function of row number, n | 3-14 |
| Figure 3.6-1 | Empirical exceedance probability within a debris event, x-direction (cross-shore) and y-direction (alongshore), for: (A) the largest applied impulse in the x-direction $I_{0,x}$; (B) the second largest applied impulse in the x-direction $I_{0,x}^{2nd}$; (C) the largest applied impulse in the y-direction $I_{0,y}$; and (D) the second largest applied impulse in the y-direction $\bar{I}_{0,y}^{2nd}$ (orange markers indicate a current-only condition) | 3-16 |
| Figure 3.6-2 | Empirical exceedance probability within a collision event, x-direction (cross-shore) and y-direction (alongshore), for: (A) the largest applied impulse in the x-direction $I_{0,x}$; (B) the second largest applied impulse in the x-direction $I_{0,x}^{2nd}$; (C) the largest applied impulse in the y-direction $I_{0,y}$; and (D) the second largest applied impulse in the y-direction $\bar{I}_{0,y}^{2nd}$ (orange markers indicate a current-only condition) | 3-17 |

- Figure 3.7-1 Comparison of maximum load, x-direction (cross-shore) and y-direction (alongshore), from Equation 3.7-2 and experimental peak loads: (A) M-LC-1, x-direction; (B) M-LC-1, y-direction; (C) I-LC-1, x-direction; (D) I-LC-2, x direction; (E) I-LC-3, x-direction; (F) I-LC-4, x-direction; and (G) I-LC-5, x-direction..... 3-19
- Figure 3.7-2 Plot of maximum experimental debris impact loads versus exceedance probability for a row 1 (unsheltered) structure, compared with the value from Equation 3.7-7 (adapted from ASCE 7-22 Chapter 5 for flood loads) and the value from proposed Equation 3.7-11, with $I_0 = p_n$, $C_I = 1$, $C_B = 1$, and $C_D = 1$ 3-24
- Figure 4.1-1 Plan view showing offset buildings in a simplified building array (as compared to Figure 1.1-1)..... 4-2
- Figure 4.4-1 Plan view showing the location of typical debris impacts throughout the building array..... 4-7
- Figure A.1-1 Relative wave height, H/H_i , for reflected waves on the landward face of a building in a given row, as a function of gap ratio, r A-4

List of Tables

| | | |
|-------------|---|------|
| Table 3.7-1 | Dynamic Response Coefficients R_{max} from ASCE 7-22, Recast as C_{Rmax} | 3-21 |
| Table 3.7-2 | Comparison of Maximum Impulsive Debris Load Equations, in the Direction of Waves and Current Flow, for First Row Structures, Risk Category II Importance, Deep Unobstructed Flow, and Zero Damping | 3-22 |
| Table A.1-1 | Wave Energy Transmission Through a Building Array as a Function of Rows and r | A-2 |

Chapter 1

Introduction

The design of buildings subjected to coastal inundation is a two-step process. Step one is to establish flood hazards at the building site, and step two is to calculate flood loads on the building using those flood hazards. This report presents the results of a series of experimental and numerical studies of wave and current flow through a simplified building array, evaluates the results in the context of flood design practice and the state of knowledge available in the literature, and recommends possible improvements to engineering practice related to coastal flooding in developed regions and possible changes to flood load provisions in building codes and standards.

Design for coastal inundation is a two-step process:

- Establish flood hazards at the site.
- Calculate flood loads using flood hazards at the site.

In the context of this report, flood hazards include:

- Water Depth
- Overland Flow (Current) Velocity
- Overland Wave Conditions
- Floodborne Debris Object Characteristics

and flood loads include:

- Hydrostatic Loads¹
- Hydrodynamic Loads
- Wave Loads
- Floodborne Debris Impact Loads

1.1 Problem Statement and Motivation

The design of buildings in areas subject to flooding requires knowledge of design flood conditions and of loads induced by flooding and debris impact. In developed coastal regions, the size, location, and spacing of buildings, and the layout of the streets, can have a significant impact on how waves, current, and debris propagate throughout the region. Computation of overland storm wave and tsunami flow using a bare-earth assumption (i.e., buildings and

¹ Hydrostatic loads are well understood, and will not be considered in this report. Discussion will focus on waves, current, and debris, and their associated loads on buildings.

Better estimates of wave, current, and floodborne debris effects are needed in developed regions subject to coastal inundation events.

other obstacles are not present, and inundation is computed over open ground) is widely believed to introduce errors and additional uncertainty into estimates of hydrodynamic conditions and structural load calculations.

Better estimates of flood hazards and flood loads are needed in developed regions subject to coastal inundation events. Specifically, better estimates of wave, current, and floodborne debris effects, and more information on how the presence of buildings and other obstacles changes the hydrodynamic behavior, would benefit the vast majority of design projects that do not have the benefit of site-specific hydrodynamic modeling.

Figure 1.1-1 shows a simplified building array, representing a hypothetical coastal region, and defines key terms used in this report.

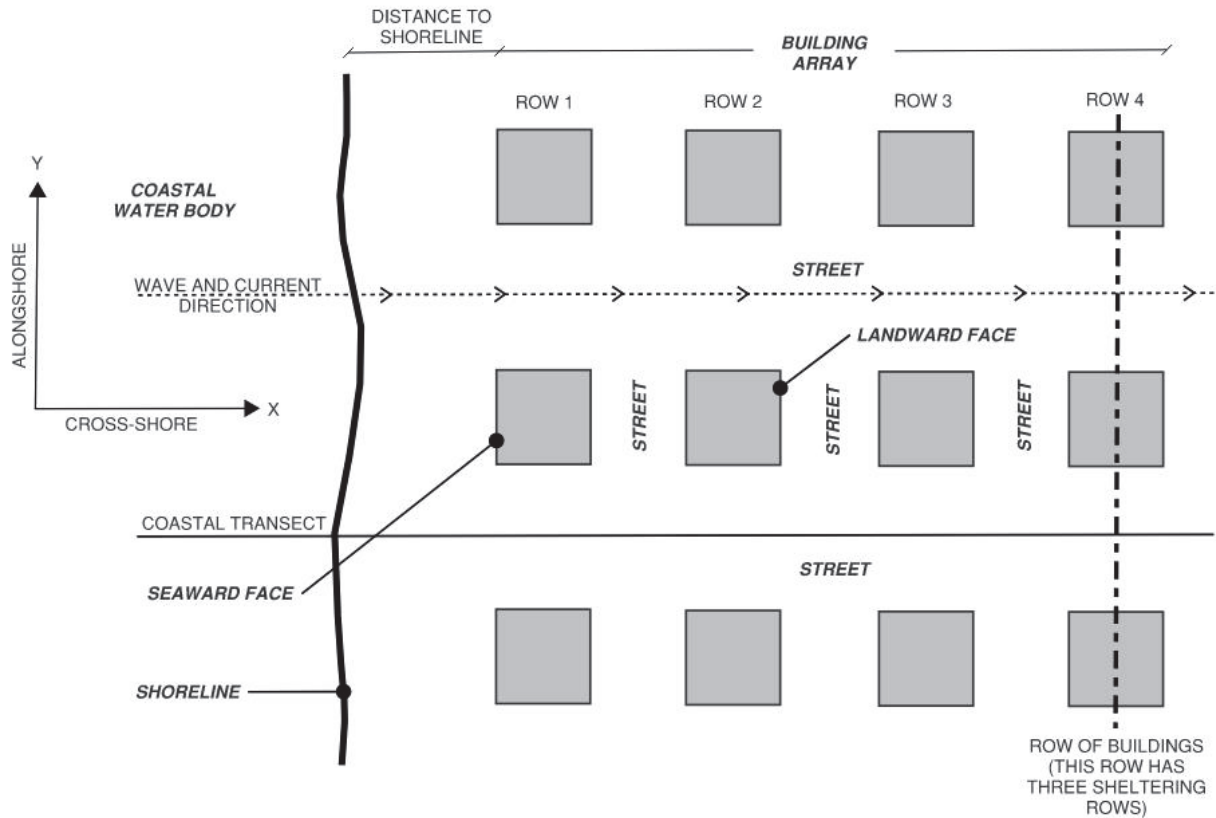


Figure 1.1-1 Plan view showing simplified building array and definitions of key terms.

Of particular interest is how coastal flood hazards and loads on buildings vary throughout a developed urban area. Questions that designers might have related to this scenario include:

- How do flow depths and velocities vary throughout a building array?
- How do hydrostatic and hydrodynamic loads vary throughout a building array?

- How do wave heights vary throughout a building array, and how do these compare with the wave reduction procedures in the literature?
- How do wave loads vary throughout a building array?
- How do floodborne debris objects pass through a building array and where are debris impacts likely to occur?
- How do debris impact loads vary throughout a building array?
- How do flood loads vary on each face of an individual building within a building array?
- Can flood hazards and loads within a building array be expressed as a function of hazards and loads based on bare earth conditions?
- Can flood hazards and loads within a building array be expressed as a function of flood hazards and loads at the seaward-most row of buildings in the array?

1.2 Project Overview and Approach

The ATC-149 Project was funded by a grant from the National Institute of Standards and Technology (NIST), through the University of Notre Dame. The purpose of this project was to support a multi-year research effort on *Coastal Inundation Events in Developed Regions* being performed at the University of Notre Dame. Work included the formation of a Project Oversight Committee of practicing engineers and researchers with expertise in coastal engineering and flood design to review and advise on the research plan, and to assist in the translation of results into engineering practice.

A key outcome of the work includes recommendations on how results from experimental and numerical studies might be used to:

- Improve or enhance present design practice
- Improve flood design provisions in building codes and standards

Intended outcomes of the work include recommendations on how experimental results might be used to:

- Improve or enhance present design practice.
- Improve flood design provisions in building codes and standards.

1.3 Description of Present Design Practice

Present U.S. practice for estimating flood hazards and flood loads varies depending on project size, design budget, designer expertise, and Authority Having Jurisdiction (AHJ) requirements. Practice varies from simple, conservative approaches to more sophisticated estimates of flood hazards and loads at a project site. Once flood hazards are determined, design loads are calculated using equations contained in building codes, standards, and other guidance.

Present design practice can be characterized as one of the following approaches:

- Simple Approach
- Enhanced Approach
- Site-Specific Modeling Approach

Present design practice can be characterized as one of the following design approaches of varying levels of complexity:

- **Simple Approach.** Designers: (1) obtain flood depth from, or based on, Federal Emergency Management Agency (FEMA) Flood Insurance Rate Map (FIRM), Flood Insurance Study (FIS) or AHJ flood elevation requirements; (2) estimate flow velocity at the project site based on the flood depth (by using conservative equations in standards or other guidance, and assuming the flow could come from any direction; (3) assume depth-limited breaking waves at the site approaching from any direction; and (4) assume debris objects present in the vicinity of the shoreline could reach the project site and strike any building face at the flow velocity estimated above. *Designers are most likely to use this approach.*
- **Enhanced Approach.** Designers combine knowledge of the flood source and surrounding local features, including nearby buildings, with engineering judgement to improve estimates of flow depths, velocities, wave heights and directions, and likely debris impacts at the project site. Designers could elect to: (1) reject the conservative assumption that waves, current, and debris can strike from any direction, and instead limit the directions considered based on the street layout and nearby building characteristics; (2) create new WHAFIS (Wave Height Analysis for Flood Insurance Studies) transects at or near the project site to better estimate local wave conditions; (3) use flow continuity and blockage by buildings and other obstructions to adjust local flow velocities that were based on depth alone; and (4) screen out large debris objects that are unlikely to pass through the building array. *Some designers and some projects use this approach.*
- **Site-Specific Modeling Approach.** Designers use more sophisticated analytical, numerical, or experimental modeling of waves, current, and debris through the building array. Flood hazards and flood loads for waves, current, and debris are calculated or measured at points of interest throughout the array. *This approach would likely be reserved for the largest projects and most important buildings.*

At present, design practice is limited by the ability to accurately specify flood hazards and the ability to accurately calculate flood loads once flood hazards are specified.

1.4 Resources for Present Design Practice and their Limitations

Design practice generally relies on sources for flood hazard information and flood load requirements described in the following sections. At present, practice is limited by the ability to accurately specify flood hazards and the ability to accurately calculate flood loads once flood hazards are specified.

1.4.1 Flood Hazard Maps and Studies

For establishing flood hazards, designers commonly refer to a community-adopted flood hazard study and map, most often the Federal Emergency Management Agency (FEMA) Flood Insurance Rate Map (FIRM) and Flood Insurance Study (FIS). The FIRM and FIS generally define the area subject to flooding under the 1-percent annual chance flood, also known as Base Flood or 100-year mean recurrence interval (MRI) flood, and the 0.2 percent annual chance flood (500-year MRI). The FIRM and FIS also provide information on flood elevations and wave conditions derived from FEMA model outputs. FEMA storm surge modeling is based on bare earth topographic conditions, with buildings and other obstructions implicitly represented by roughness factors. The storm surge model output is a stillwater surface from which flood elevations and depths can be obtained. FEMA overland wave conditions are based on WHAFIS (Wave Height Analysis for Flood Insurance Studies) model results (FEMA, 1981).

Wave dissipation due to the presence of buildings is represented in WHAFIS using a procedure from the National Academy of Sciences (NAS) *Methodology for Calculating Wave Action Effects Associated with Storm Surges* (NAS, 1977). The procedure approximates the actual building array as a number of rows of buildings, with a certain fraction of the alongshore length obstructed by the buildings in each row. Thus, the FIRM accounts for the presence of buildings using WHAFIS and the NAS (1977) procedure.

Unfortunately, the flood hazards within urban coastal areas are not well-described by FEMA studies and maps, and do not capture complex interactions of flood effects around closely spaced buildings. FEMA flood hazard studies and maps cover large areas, and are based on simplified depictions of land use and land cover (i.e., roughness factors in a numerical storm surge model). These models cannot explicitly account for the blockage or channelization of flood waters by and between buildings.

Flood hazards within urban coastal areas are not well-described by FEMA studies and maps, and do not capture complex interactions of flood effects around closely spaced buildings.

1.4.2 Local or State Floodplain Management Regulations

Floodplain management regulations typically provide design and construction requirements that are separate from the building code. Some floodplain regulations might be the same as building code requirements, while others might be different. Designs are required to meet the more restrictive of the two.

1.4.3 Building Codes and Standards

Codes and standards used in design practice include the building code adopted by the Authority Having Jurisdiction (AHJ), and flood-related

Flood-related codes, standards and guidance include:

- ASCE 7-22
- ASCE 24-14
- FEMA P-55 Coastal Construction Manual

standards referenced by the building code, including ASCE 7-22, *Minimum Design Loads and Associated Criteria for Buildings and Other Structures* (ASCE, 2022) and ASCE 24-14, *Flood-Resistant Design and Construction* (ASCE, 2014).

Flood load provisions in building codes and standards are fairly basic, having been developed using the philosophy that simple procedures are acceptable as long as they are conservative². Flood load provisions allow for more advanced analytical, numerical, or laboratory procedures, but few designers use such procedures. In some cases, flood load provisions do not include prescriptive load calculations, instead referring designers to principles of basic fluid mechanics.

Designers sometimes refer to other flood load calculation guidance, such as the FEMA P-55 *Coastal Construction Manual* (FEMA, 2011), which provides prescriptive load calculation procedures for certain flood conditions.

1.5 Report Organization and Content

This report presents the results of a series of experimental and numerical studies of wave and current flow through a simplified building array, evaluates the results, and recommends possible improvements to engineering practice and flood load provisions in building codes and standards.

Chapter 1 introduces the problem statement and motivation, describes present design practice, and identifies currently available resources and limitations.

Chapter 2 presents an overview of the laboratory and numerical research and summarizes experimental and analytical results.

Chapter 3 describes overarching findings from the research, compares results to solutions available in the literature, and discusses potential implications of the observed results.

Chapter 4 summarizes the practical applications of the work, and provides recommendations for improved design practice and potential future changes to flood load provisions.

Appendix A explains National Academy of Sciences wave transmission and energy concepts and extrapolates the approach to wave reflection.

A list of Symbols used throughout this report, a list of References cited, and a list of Project Participants are provided at the end of this report.

² As shown later in this report, floodborne debris impact procedures in ASCE 7-22, Chapters 5 and 6 may not be conservative.

Chapter 2

Overview of Research and Experimental Results

Laboratory results presented herein are a combination of experimental data taken at the O.H. Hinsdale Wave Laboratory Directional Wave Basin (DWB) at Oregon State University (most results), and computational data using OpenFOAM at Notre Dame University (some results). Results within a 10×10 building array of idealized cubicle structures are presented for wave, current, and wave plus current conditions, and cases with and without debris.

Experiments included tsunami-type waveforms and irregular storm waves. Tsunami waveforms are slowly varying single waves associated with the transport of large masses of water in the wave direction, while irregular storm waves are associated with oscillatory water motions and little net transport of water. Although these wave types are different, there are similarities, and generalizations are made where possible.

2.1 Experimental Set-Up

Figure 2.1-1 presents an overview of the laboratory test set-up, showing instrument and structure locations. Six of the 100 structures were instrumented to record loads. These included one with a multi-axis load cell in the first row of structures (M-LC-1), and five with single-axis load cells (in the direction of wave propagation) in the first five rows (I-LC-1 to I-LC-5). The remainder of the structures were made from uninstrumented concrete blocks. Both instrumented and uninstrumented structures were 0.4 m cubes, spaced 1.0 m in the alongshore and 0.8 m in the cross-shore directions. This could be considered a 1:25 to 1:50 scale for single family houses or small commercial buildings.

A piston-type wavemaker was used to generate waves. For some tests, currents totaling approximately $0.26\text{m}^3/\text{s}$ were generated by two pumps, creating a recirculating flow. A combination of wave gauges and current meters was used to evaluate hydrodynamics within the building array, with additional measurements taken outside the array (i.e., offshore). Free surface measurements in the wave or wave-current conditions include the effects of waves, while free surface measurements in the current-only condition represent a stillwater surface without wave effects.

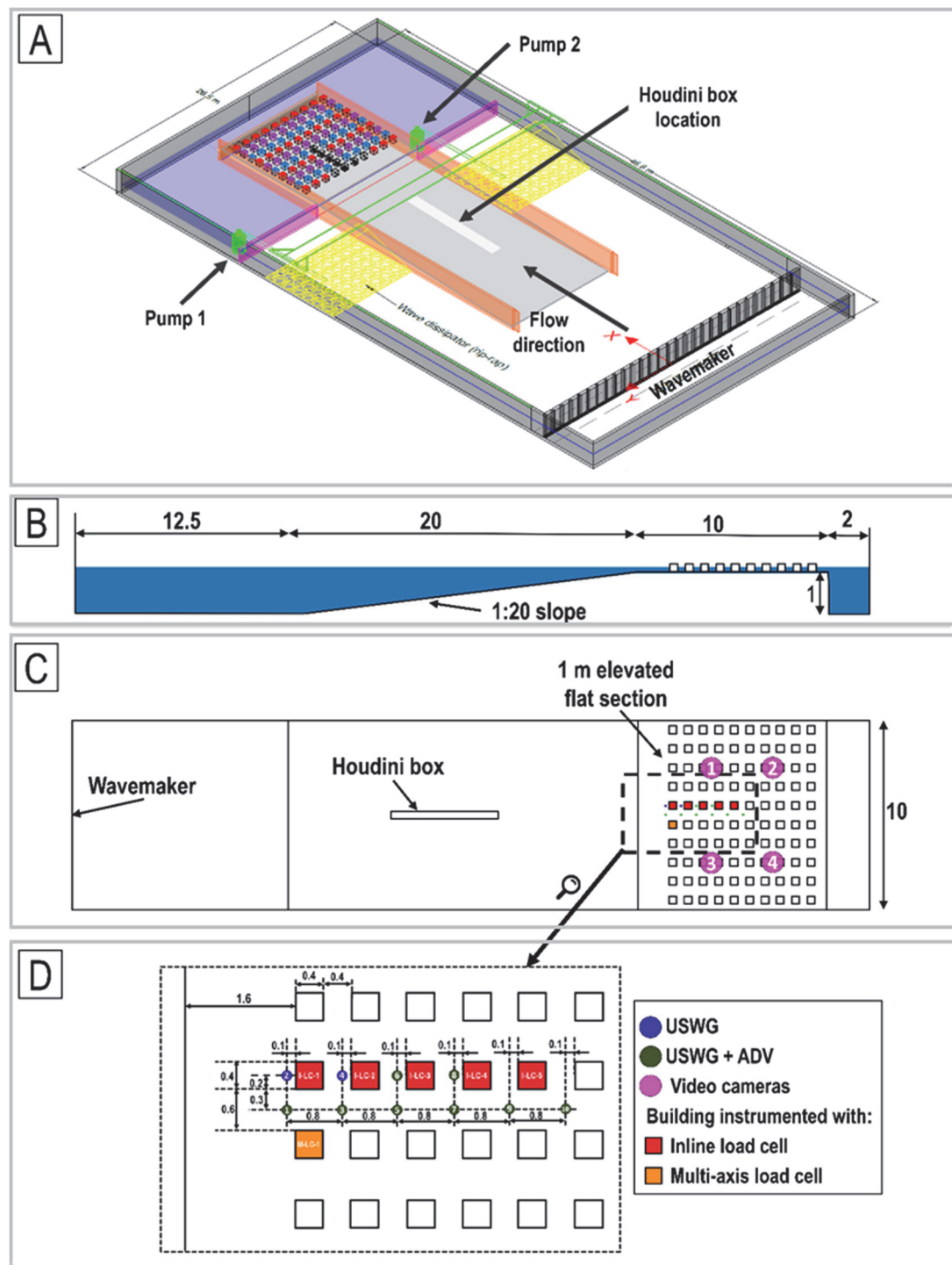


Figure 2.1-1 Experimental set-up: (A) isometric representation of the DWB; (B) cross-shore elevation view in the center of the DWB; (C) plan view of the concrete beach, including the location of the video cameras; and (D) location of instrumentation in the test section (dimensions in meters).

A more complete description of the experimental set-up can be found in Moris et al. (2021). Two main series of experiments are included here: (1)

loading on a building array using long wave (tsunami-like) runup; and (2) debris impact loading on the building array during inundated storm wave-current flow. The results for the first series of experiments are reported in Moris et al. (2021), and the results for the second series of experiments are reported in Moris et al. (2022) and Moris (2022).

Numerical tests used openFOAM, but with a 10×3 building array to decrease computational time. All results were taken at the center structure. An additional series of tests was conducted by removing the first row of buildings, then the first two rows, etc., until only the tenth row remained. Finally, numerical tests also employed bare earth simulations for comparison with typical models that do not represent individual structures. All tests had waves and currents coming from the seaward direction; thus, the *seaward* face of a structure is also the *front* face of the structure, which is more exposed to wave and debris loading. If waves and currents change direction (e.g., during outflow drainage in a tsunami or storm surge event), the *landward* face of a structure would then become the *front* face.

2.2 Wave Runup within an Array

Wave generation for experimental tests was initiated with a piston-type wavemaker. In the first 12.5 m, waves propagated over flat bathymetry to the concrete beach: first over a 20 m long, 1 m high, 1:20 constant slope, and second on a 10 m long, 1 m elevated horizontal test section. After the test section, the flow was deposited in a 1 m deep reservoir. The initial water depth was 0.98 m, which gives 0.02 m of difference between the test section bed and the initial water level. On the test section, a 10×10 building array of 100 idealized structures was placed, representing a coastal developed region. The term “row” references the cross-shore location of the structures, with row 1 referring to the group of structures located closest to the beach slope, and row 10 as the group of structures located closest to the back reservoir. The distance from the front face of the first row of structures to the beginning of the test section was 1.6 m. Tsunami-like waves were generated using a wavemaker displacement that followed an error function, with waves defined by a scale factor (e.g., Park et al., 2019). Four scale factors were used in these tests: $S_f = [2.0, 2.5, 3.0, 4.0] \text{ s}$. The lower the value of S_f , the faster the piston and the larger the wave height. Laboratory tests also generated solitary waves with heights $H = [0.075, 0.15, 0.20] \text{ m}$.

Free surface elevations for wave conditions were recorded on the 1:20 slope using nine resistance-type wave gauges (WG). Five ultrasonic wave gauges (USWG) recorded the free surface elevation in the test section and four Acoustic Doppler Velocimeters (ADV) recorded the instantaneous velocity

2 cm above the bottom in the test section. Hydrodynamic measurements were recorded at 100 Hz. USWGs and ADVs were hanging from a bridge-like structure above the test section. By sliding the bridge and repeating the wave run, data were recorded at twice the number of locations. This also allowed repeated measurements from the in-line load cells with the same wave condition, which was useful for checking the repeatability of the experiment. Details about the instrumentation placement are presented in Figure 2.1-1.

Additional numerical tests were conducted with features similar to the base case, but with a reduced (2-row) building array and a steeper beach slope of 1:10. Additionally, the initial water level was 0.75 m, and the elevation of the test bed was 0.795 m. Solitary waves with heights of 0.1 m, 0.175 m, 0.25 m, 0.325 m, 0.40 m, and 0.475 m were generated by specifying the solitary boundary condition in openFOAM, which generates a solitary wave at the location of the wavemaker according to the Boussinesq theory, as described in Higuera et al. (2013). These conditions allowed the use of a wider range of wave conditions to complement the 10-row building array simulations.

2.3 Wave Loads within an Array

In general, wave loads decreased with an increase in the number of rows providing shelter.

To evaluate the change in wave loads in the presence of a building array, recordings from five in-line load cells were used. In general, wave loads decreased with an increase in the number of rows providing shelter. Figure 2.3-1 provides an example of laboratory and computational results for rows 1 through 5, showing a decrease in wave load with an increase in the number of sheltering rows, as well as good agreement between laboratory and computational results.

Three load reduction factors ($LRFA_n$, $LRFB_n$, and $LRFC_n$) were defined to isolate and evaluate the changes in wave runup loads within an array. Using the force quantities illustrated in Figure 2.3-2, the load reduction factors are defined as:

$$LRFA_n = \frac{F_{n,\max}}{F_{n,\max}^{(0)}} \quad (2.3-1)$$

$$LRFB_n = \frac{F_{n,\max}}{F_{0,\max}} \quad (2.3-2)$$

$$LRFC_n = \frac{F_{n,\max}}{M_{BE,\max}} \quad (2.3-3)$$

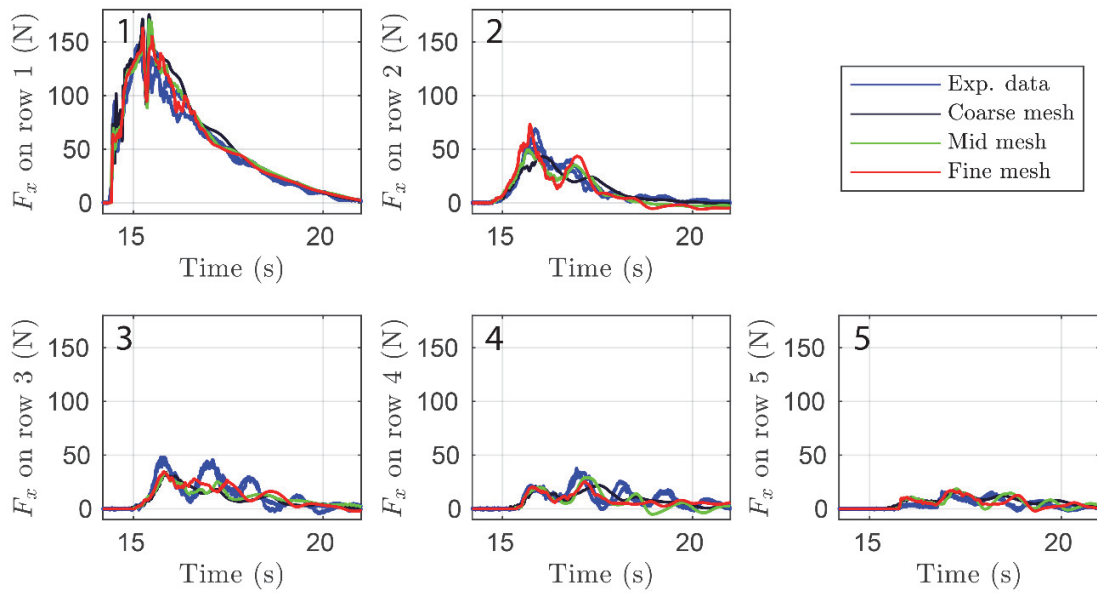


Figure 2.3-1 Example of laboratory and computational loading for rows 1-5.

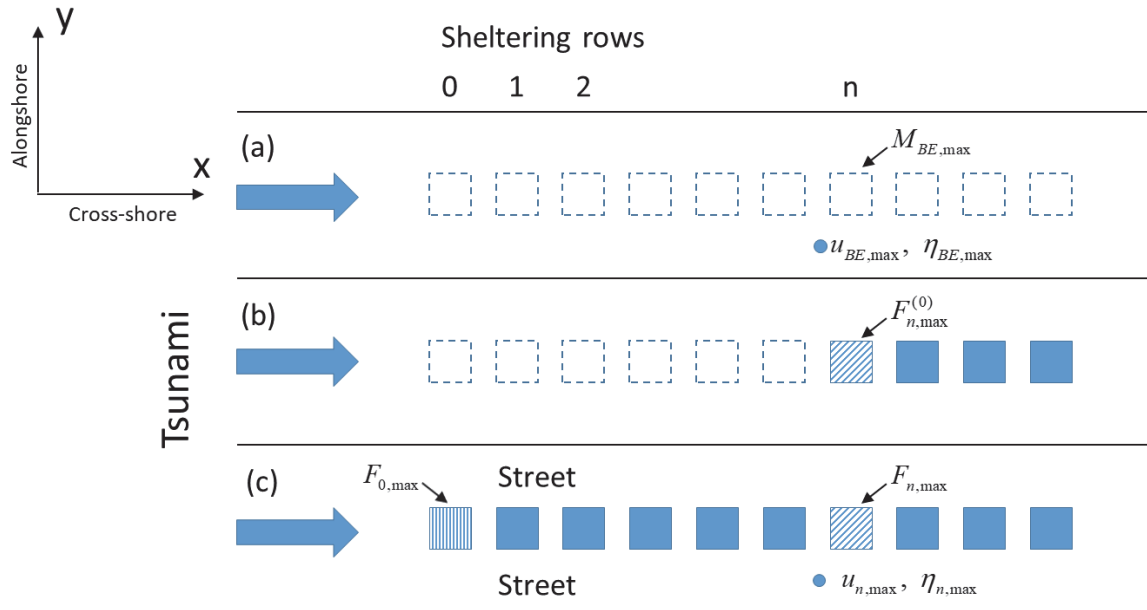


Figure 2.3-2 Illustration of important load quantities in three cases: (a) bare earth simulation with all structures removed for maximum momentum flux, velocity, and surface elevation; (b) unobstructed load on a structure in an array with n sheltering rows removed; and (c) sheltered load case with n sheltering rows in place.

Figure 2.3-3 shows laboratory and computational results for $LRFA_n$, $LRFB_n$, and $LRFC_n$, including additional results from other laboratory experiments for $LRFB_n$ (e.g., Tomiczek et al., 2016; Sogut et al., 2019; and Moon et al., 2019).

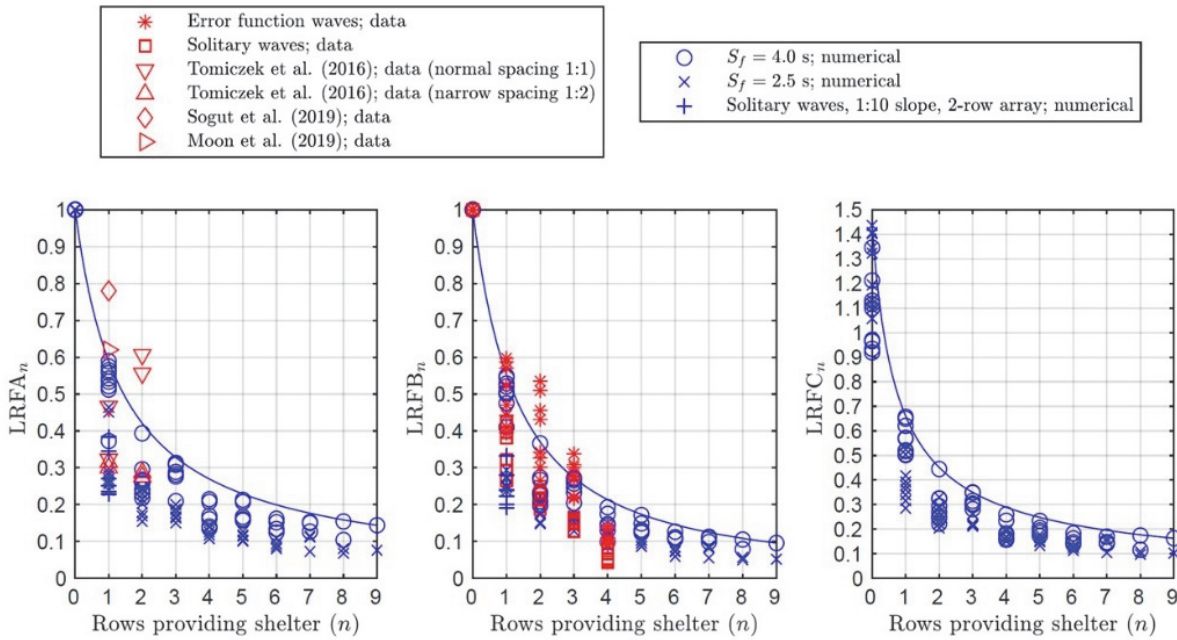


Figure 2.3-3 Numerical and experimental Load Reduction Factors $LRFA_n$, $LRFB_n$, and $LRFC_n$ as a function of the number of rows providing shelter, n .

$LRFA_n$ is a measure of the change in maximum load due to sheltering at a location, defined as the ratio between the maximum wave loading on a structure with n rows of structures providing shelter ($F_{n,\max}$), Figure 2.3-2c, and the load when all n sheltering rows are removed ($F_{n,\max}^{(0)}$), Figure 2.3-2b. Note that to obtain the ratio $LRFA_n$, two simulations are required: one with an unsheltered structure at a given location, and one with a building array providing n rows of shelter.

$LRFB_n$ measures the ratio between the maximum wave loading on a structure with n rows of shelter, ($F_{n,\max}$), Figure 2.3-2c, to the maximum unobstructed wave loading on the frontmost structure in the array ($F_{0,\max}$), Figure 2.3-2c. Although $LRFB_n$ does not give a direct measurement of the change in maximum load at a given location, it can be calculated using the results from a single laboratory experiment or one computational run. This is particularly useful when dealing with data from laboratory experiments, since modifying the setup is not as straightforward as it is for numerical experiments.

$LRFC_n$ measures the ratio between the maximum wave loading on the structure with n rows of shelter ($F_{n,\max}$), Figure 2.3-2c, to the maximum bare earth momentum flux ($M_{BE,\max}^{(l)}$) at the same location, Figure 2.3-2a. $LRFC_n$ is introduced because the calculation of load reduction factors $LRFA_n$ and $LRFB_n$ needs an estimate for an unobstructed load. To estimate wave loading on a structure it is necessary to place the actual structure in the numerical

domain and to vertically solve the flow hydrodynamics, requiring a large amount of computing power. However, it is possible to obtain bare earth momentum flux from simpler averaged models that do not necessarily require representation of the structure with high resolution. Therefore, $LRFC_n$ is a useful load reduction factor because it can be multiplied by $M_{BE,\max}$ to obtain an estimate of the maximum sheltered wave loading.

2.4 Debris Impact within an Array

Debris experiments used the same experimental setup, measuring debris transport and debris loading in wave-current and current-only flow conditions. In all tests, the initial stillwater depth was 1.1 m, giving a water depth of 0.1 m on the elevated test section. Two pumps on each side of the DWB generated a constant flow of approximately $Q = 0.26 \text{ m}^3/\text{s}$ for all tests. Two hydrodynamic conditions were tested. The main hydrodynamic condition consisted of random waves over a constant current (wave-current condition), in which random waves were generated by a piston-type wavemaker following a TMA spectrum with a peak period $T_p = 2.25 \text{ s}$ and a significant wave height of $H_s = 0.2 \text{ m}$. Supplemental tests with a constant flow of approximately $Q = 0.26 \text{ m}^3/\text{s}$ with no waves (current-only condition) were also conducted.

Wooden debris with dimensions of $15 \text{ cm} \times 15 \text{ cm} \times 1.9 \text{ cm}$ and an average soaked mass of $m_d = 359 \text{ g}$ were released from a box (i.e., Houdini box) above the sloped section in the center of the concrete beach. For the wave-current condition, 30 trials were conducted. In each trial, 39 individual debris elements were released, for a total of $N_t = 39 \times 30 = 1170$ debris elements. For the current-only hydrodynamic condition, 4 trials were conducted, and a total of $N_t = 39 \times 4 = 156$ debris elements were released. Four high-resolution video cameras were mounted on a steel frame located above the flat test section. The combined visual field allowed coverage of the entire test section so it was possible to visually track all individual debris elements.

The debris loading on the structures in the array was recorded. As in the experimental setup for wave loading, there were two different types of load cells: one multi-axis load cell (designated M-LC-1) was placed in row 1 (i.e., the row directly exposed to the wave-current action) and five (5) inline load cells (designated I-LC-n, where n is the row number) were placed in the first five rows of the building array (see Figure 2.1-1d). The M-LC-1 cell measured the structural loading response of the wave and debris action in three spatial directions for both forces and moments. The I-LC-n cells were constrained to move in only the cross-shore direction, so they recorded the structural response in terms of force only in this direction. The structural

response of the load cells was recorded at 1,000 Hz. The remainder of the structures were not instrumented.

The collision probability and the collision magnitude were assessed using both the video and the load cell recordings. A *debris event* in row n is defined as an individual debris element passing through row n within the building array, regardless of whether this debris collides with any structure located in row n . A *collision event* in row n is defined as an individual debris element impacting at least once on a structure located in row n within the building array. If the same debris element impacts a structure more than once it is still treated as one collision event, but a subsequent impact on a different structure would be considered a new collision event.

The load cells do not provide a direct record of the debris load-time history on the structure; instead, they provide the structural response to this loading in the form of cross-shore base shear (I-LC) or cross-shore and alongshore base shear (M-LC-1). Differences between these measured quantities and the raw debris load arise because a structure has finite mass, stiffness, and damping; thus, impulsive debris loads on the front face of a structure are modified by the structure response to arrive at the measured response. The analysis presented herein uses the measured loads recorded at the base of a structure to estimate the applied debris impulse on the front face. The structural response in the cross-shore direction of the instrumented structures is estimated using a standard single-degree-of-freedom (SDOF) system (see section 3.7.1). It should be noted that overturning moment was not considered because response was resonant even without debris, which prevented separation into flow and debris loading components. The torsional moment was similarly not considered.

The impact load experienced by a structural system or component is a function of not only the debris impulse, but also the properties of the structure.

Ultimately, an estimate of the debris impact design load is needed for a particular structural system or component of interest. One of the most important results from this experimental work is to emphasize that the impact load experienced by a structural system or component is a function of not only the debris impulse, but also the properties of the structure.

Chapter 3

Implications and Limitations of Experimental Results

Results of laboratory and computational experiments provide insight into wave and debris loading within a building array and can be compared with results available within the literature and engineering analyses. This chapter examines results for wave, wave-current, and current-only experiments described in Chapter 2 in more detail, attempts to contextualize results within the larger field, and illustrates both the implications and limitations of the work.

3.1 Wave Transmission

Laboratory tests show that wave loads on buildings within a rectangular array are reduced when they are sheltered by seaward rows of buildings. The reduction increases with the number of rows providing shelter. The reasons behind the load reduction are two-fold. Waves impacting a row of buildings are partially reflected or dissipated when they encounter a structure, but are largely unaffected as they pass between structures. Waves and overland currents are then channelized into the gaps between structures. This results in the largest waves and currents occurring in the cross-shore streets between buildings in an array.

In this section, the variation of wave loads within an array is discussed, and laboratory results are compared to the long-standing National Academy of Sciences (NAS) formula for wave height reduction (NAS, 1977). Because the laboratory data are limited to results from a single geometric layout of buildings with fixed spacing and uniform size, the ability to generalize results to other geometries is limited.

Experimental results are compared to the long-standing National Academy of Sciences (NAS) formula for wave height reduction (NAS, 1977).

The wave height transmitted past a row of buildings along a shoreline depends on the nature of the buildings and the alongshore spacing (NAS, 1977):

$$H_t = BH_i \quad (3.1-1)$$

where:

$$B = r^{n/2} \quad (3.1-2)$$

where H_i is the wave height incident on the first (seaward) row of buildings, and H_t is the wave height past the buildings. The transmission coefficient, B , is a function of r , which is the ratio of total open distance (gap) between buildings to the total distance measured parallel to the shoreline at the site of interest, and n , which is the number of seaward rows of buildings providing shelter to the site of interest. For a rectangular array of equal-width buildings, r is the ratio of the alongshore gap between the buildings and the center-to-center spacing of the buildings (gap plus building width).

The NAS formula in Equation 3.1-1 is used by FEMA in their WHAFIS wave propagation model for calculating wave heights along a coastal transect (FEMA, 1981). The NAS formula comes from a wave energy argument, which is described in more detail in Appendix A.

Figure 3.1-1 plots the transmission coefficient, B , as a function of the number of seaward rows of buildings, n , and different values of the gap ratio, r . In the figure, it is clearly evident that the transmission coefficient decreases with an increase in the number of seaward rows of buildings, and a decrease in the alongshore gap between buildings (smaller values of r). The horizontal line at the top of the figure, representing 100% open space, implies that no buildings are present and 100% transmission of waves.

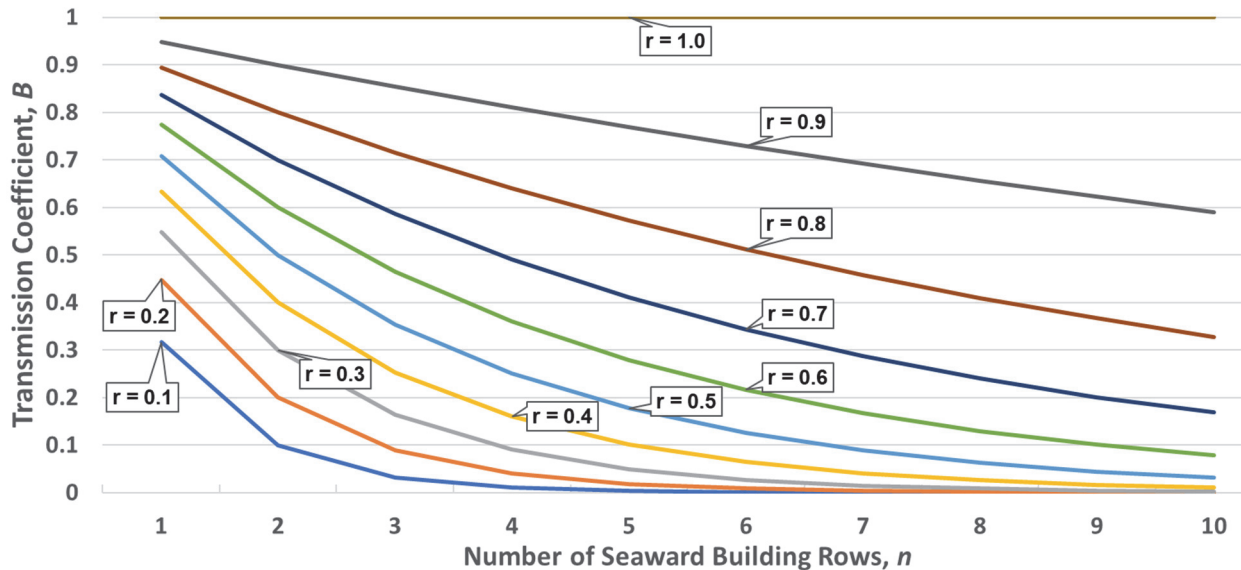


Figure 3.1-1 NAS transmission coefficient, B , as a function of the number of seaward rows of buildings, n , and gap ratio, r .

The NAS formula does not depend on the cross-shore distance between rows of buildings, but it should. Application of the conservation of energy argument assumes a uniform wave crest attacking each row, while immediately landward of the row, the waves only exist in the gaps between

buildings. Wave diffraction occurs at the gaps attempting to spread the wave energy laterally into another uniform wave crest. If the cross-shore distance between rows is only equivalent to a few building widths, the buildings in the next landward row are in the shadow of the buildings in the seaward row. Wave shadowing is perceptible for about six building widths in the wave direction and is discussed later in this chapter.

For the experiments with a 10×10 array of cubical structures, the r value was 0.6 (each building has a shorefront width of 0.4 m and the gap between adjacent buildings is 0.6 m), so the curve for $r = 0.6$ in Figure 3.1-1 is the appropriate curve for comparison with experimental results. The relative blockage ratio, w^* , is defined as the width of the building divided by the sum of the gap and the building width. In the language of NAS (1977), w^* is defined as the total frontage of the structures divided by the alongshore length of the community. The blockage ratio, w^* , is related to the gap ratio, r , by the equation $w^* = 1 - r$, and for the laboratory experiments, $w^* = 0.4$.

To relate the NAS formula to loads, the wave load is assumed to be proportional to the square of the wave height. This follows from the expression for the hydrodynamic drag force on a building, $F_D = 0.5\rho C_D u^2 A$ (Yeh, 2006), where ρ is the density of water, u is the wave velocity, C_D is the drag coefficient, and A is the building frontal area impacted. Using linear shallow water wave theory, $u_{\max} = 0.5Hc/h$, where H is the wave height, c is the shallow water wave celerity, and h is the water depth, the equation for drag force becomes $F_{D,\max} = 0.25\rho g C_D H^2 A$. Substituting the NAS formula for H , yields:

$$F_{D,\max}(n) = 0.125\rho g C_D H_i^2 r^n A / h \quad (3.1-3)$$

where all terms are as previously defined. If this load is normalized by the load in the first row, the wave load on a building can be shown to decrease with r^n through the building array:

$$F_{D,\max}(n) = r^n \quad (3.1-4)$$

where n is the number of rows of buildings seaward of the site of interest.

This ratio is effectively a load reduction factor (*LRF*) that is derived from the NAS transmission coefficient. It can be compared with experimental values of $LRFB_n$, described in Section 2.3, and is plotted versus experimental data for a value of $r = 0.6$ in Figure 3.1-2. In the figure, the NAS-derived load reduction factor agrees with the upper envelope of experimental data for up to 4 rows of sheltering. Beyond 4 rows, the data indicate somewhat higher

Wave loads are assumed to be proportional to the square of the wave height.

values of LRF (i.e., less load reduction) than the NAS transmission coefficient would imply.

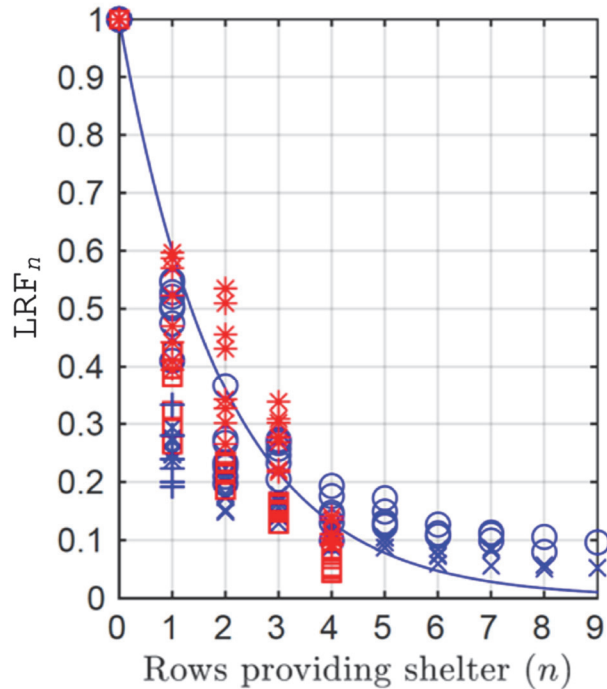
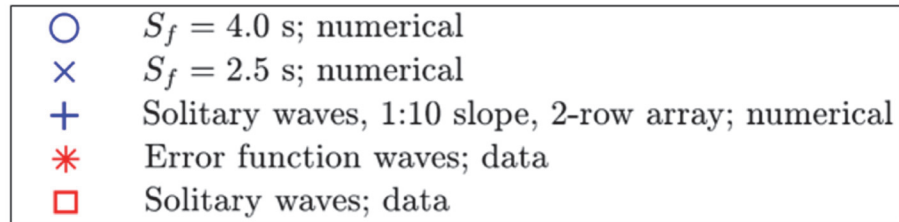


Figure 3.1-2 Load Reduction Factor (LRF) derived from the NAS transmission coefficient (solid line), as a function of the number of rows of buildings providing shelter, n , plotted along with experimental data ($r = 0.6$).

Because Figure 3.1-2 shows that the NAS-derived load reduction factor is a reasonable match to experimental data, Equation 3.1-4 can be used to generalize experimental results for building arrays with different values of r . To use experimental data to estimate LRF for building arrays with different values of r , the following relation can be used:

$$LRF = LRF_{ND} (r / 0.6)^n \quad (3.1-5)$$

where LRF_{ND} is the factor for the geometry of the current experimental array.

In Figure 3.1-3, the load reduction factor derived from the NAS transmission coefficient is plotted for different gap ratios, r . For the geometric

configuration studied ($r = 0.6$), it appears that a theoretical load reduction derived from the NAS transmission coefficient is reasonable and conservative up to $n = 4$, but is potentially unconservative when compared to experimental data beyond $n = 4$. As a result, theoretically derived values of LRF shown in Figure 3.1-3 should not be taken less than the values shown for $n = 4$ (vertical line in the figure), until experimental studies of additional geometries determine that additional conservatism is not warranted in cases with additional rows of sheltering.

The theoretical load reduction derived from the NAS transmission coefficient is conservative up to $n = 4$, but potentially unconservative beyond $n = 4$.

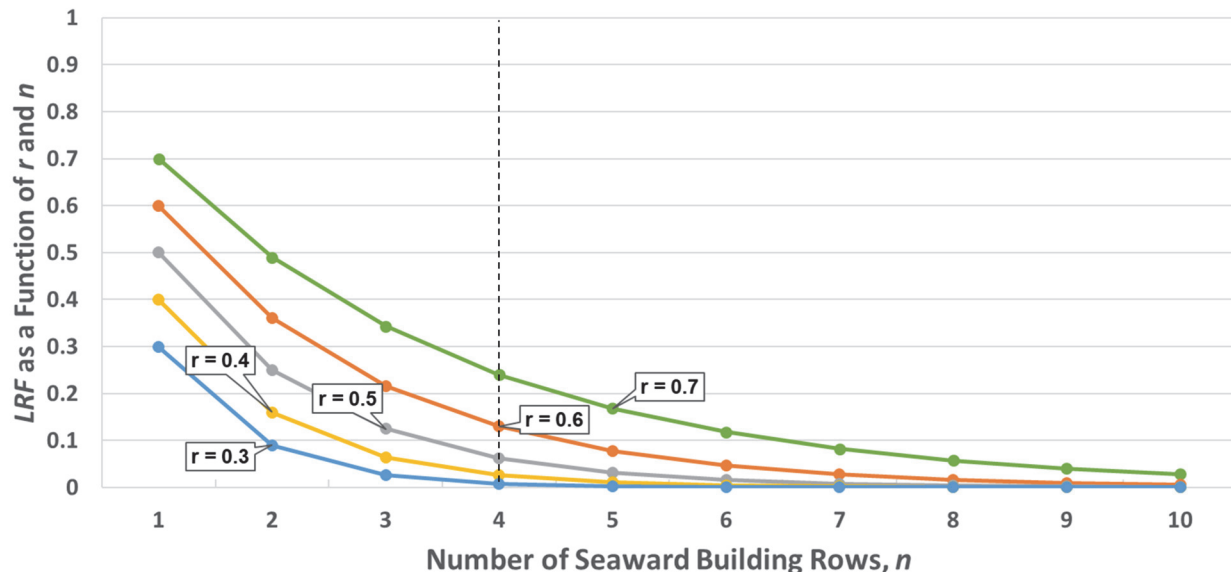


Figure 3.1-3 Load Reduction Factor (LRF) derived from the NAS transmission coefficient, as a function of the number of seaward rows of buildings, n , and gap ratio, r .

3.2 Wave Load Effects Due to Row Spacing, Distance from Shoreline, and Lateral Building Offsets

In addition to the gap ratio, r , other factors affect the magnitude and distribution wave loads within a building array. These include the alongshore and cross-shore spacing between buildings, the distance between the location of interest and the shoreline, the alignment of the buildings, and whether the buildings in an array are offset between adjacent rows. The boundary conditions at the landward end of the building array, as well as the uniformity (or variation) in size of buildings within the array can also affect results.

Some of these factors were explored in the laboratory, while others were modeled numerically by Moris et al. (2021). Figure 3.2-1 (from Moris et al., 2021) shows a visual comparison between a laboratory wave as it hits the first row of buildings and results from the numerical model. The dark streaks (shadows) behind the buildings that are visible in the numerical model are

the result of sheltering (shadowing) provided by seaward rows of buildings. The sections that follow explore the effects of each of these factors on wave loads in an array.

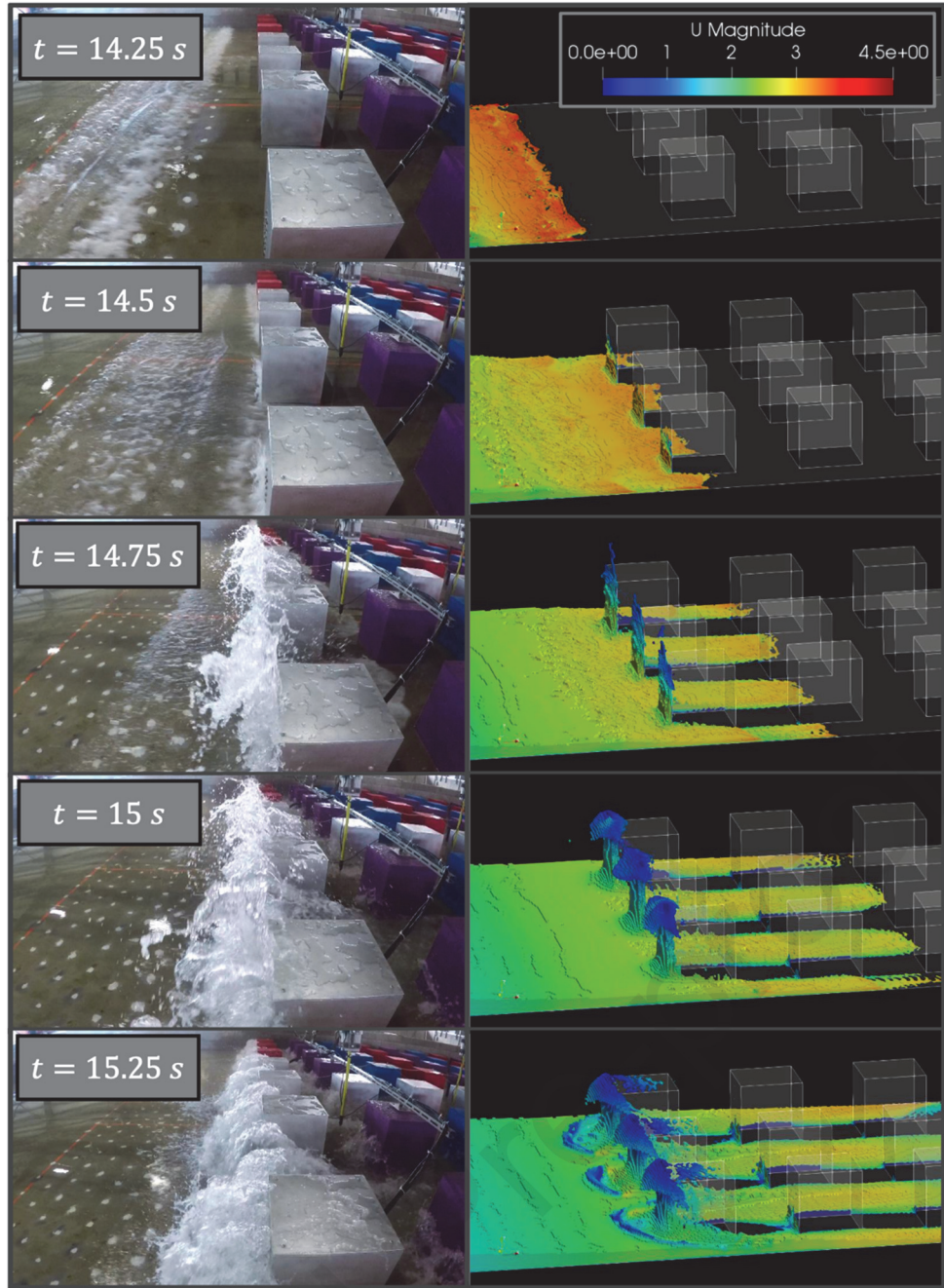


Figure 3.2-1 Comparison of laboratory video and numerical modeling results (Moris et al., 2021).

3.2.1 Alongshore Spacing of Buildings

The gap ratio, r , is a function of the alongshore spacing of buildings. For a given row, the wave load on a structure is proportional to r^n , where n is the

number of seaward rows (i.e., for row 2, $r^n = r^1$ as there is one seaward row). The blockage ratio, w^* , is related to the gap ratio, r , by the equation $w^* = 1 - r$. Moris et al. (2021) numerically examined the effect of spacing for two different tsunami waves, with results shown in blue in Figure 3.2-2. NAS formula results are indicated in red (symbol \times). In the figure, results show a decrease in LRFA with an increase in blockage ratio for the two types of tsunami waves, $S_f = 2.5\text{ s}$ (symbol \times) and 4.0 s (symbol \circ). The simple NAS model agrees reasonably well numerical data, and in all cases but one, provides an upper bound for the numerical results.

As the blockage ratio increases, wave load reductions increase, and load reduction factor decreases.

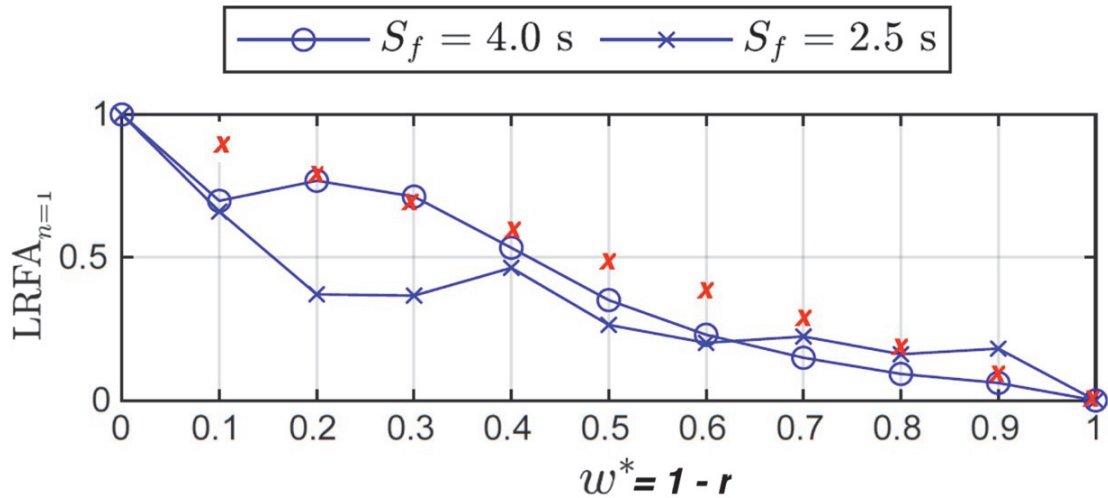


Figure 3.2-2 Plot of $LRFA$ versus blockage ratio, w^* , showing the effect of building spacing on wave loads in row 2; numerical results from Moris et al. (2021) shown in blue for two different tsunami waves (symbols \circ and \times), and NAS load reductions shown in red (symbol \times).

3.2.2 Cross-Shore Spacing of Rows

Buildings exposed to waves cast a shadow on the area behind them. This shadowing is readily seen in the tests of Yang et al. (2018). In Figure 3.2-3, a wide structure reduces the tsunami wave height impinging on the landward structure behind it. A similar sheltering effect occurs for buildings in currents, as the flow goes around the building creating a sheltering wake with a reduced water level downstream.

Shadowing is also visible in the experimental results from Moris et al. (2021), as shown in Figure 3.2-1. Most of the wave action and fluid flow is channeled between the buildings (into the shore-normal streets). In the second row, very little water impacts the buildings.

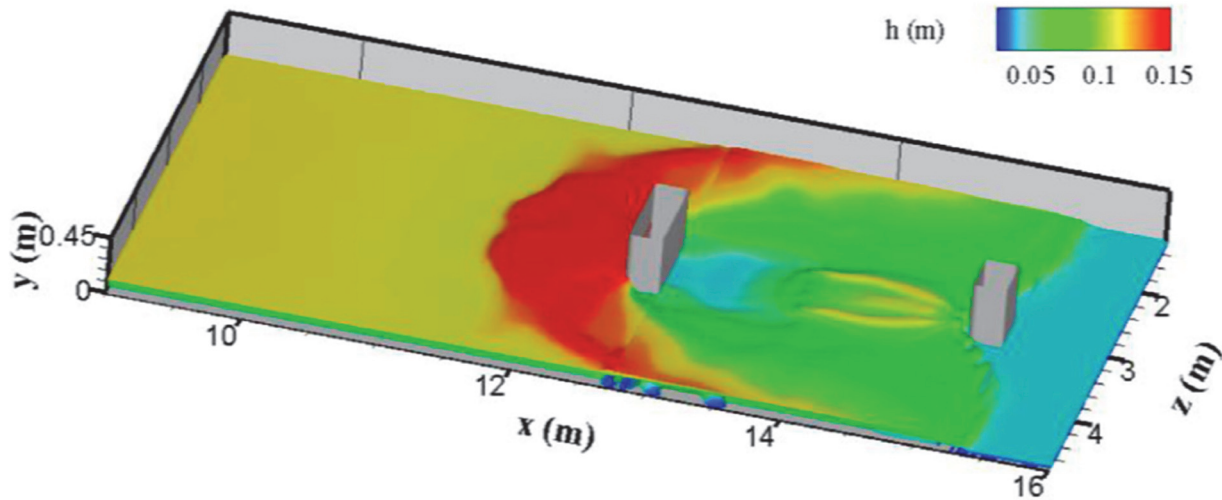


Figure 3.2-3 Tsunami water surface elevations around two coastal structures. The redder the color the deeper the water. The seaward structure on the left blocks most of the wave and provides a protective shadow for the landward structure behind it (from Yang et al., 2018, with permission).

As the cross-shore spacing between the rows increases, wave load reductions decrease, and load reduction factor increases.

Defining d as the distance between rows, Moris et al. (2021) numerically examined the effect of nondimensional distance $d^* = d/b$ for row 2, where b is the width of the structures. (In the laboratory experiments, d^* was fixed at 1.0, but in the numerical model, the ratio was varied.) Results are shown in Figure 3.2-4. The beneficial blocking effect of the first row of buildings decreases as the cross-shore spacing between the rows increases (e.g., $LRFA$ increases by 50% as d^* increases from 1.0 to 2.5. Conversely, $LRFA$ decreases as the spacing between rows decreases, approaching zero as d^* goes to zero.

\circ $S_f = 4.0$ s \times $S_f = 2.5$ s

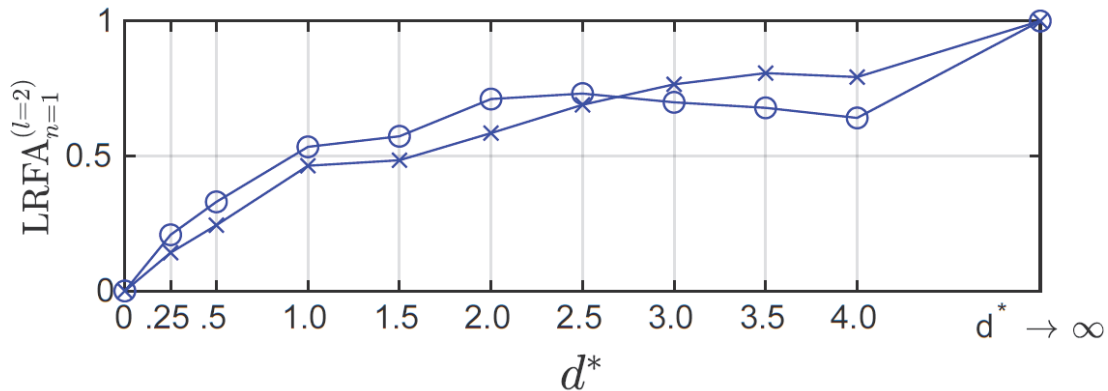


Figure 3.2-4 Plot of $LRFA$ versus nondimensional distance between rows, d^* , showing the effect of row spacing on wave loads in row 2, for $w^* = 0.4$.

3.2.3 Distance from the Shoreline

Wave height, and the impact of impinging waves is diminished with increased distance from the shoreline. It is possible to determine this effect from the numerical modeling in Moris et al. (2021), by calculating the ratio of $LRFB_n / LRFA_n$, which yields the ratio, $F_{n,\max}^{(0)} / F_{0,\max}$, or the load on a building at a given location assuming all sheltering rows have been removed, divided by the load at row 1 (see Figure 2.3-2). This ratio gives the load reduction on the first row of buildings as the location moves inland.

As the distance from the shoreline increases, wave heights and wave loads diminish.

Figure 3.2-5 plots $LRFB_n$, $LRFA_n$, and their ratio, versus n . The fact that the ratio (upper line in the figure) is less than unity demonstrates the decay of the wave impact load with distance from the shoreline. For example, at a location in row 10 ($n = 9$), a ratio of 0.66 indicates a 34% reduction in load due to distance from the shoreline.

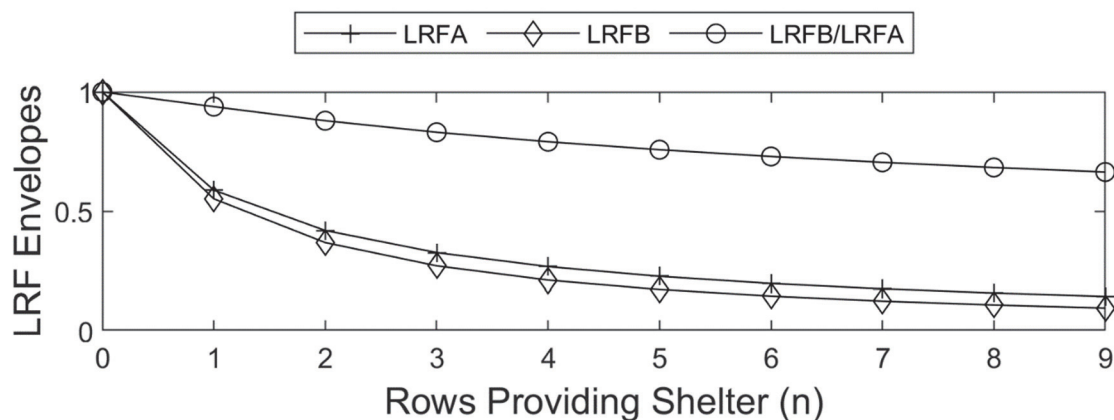


Figure 3.2-5 Ratio of Load Reduction Factors, $LRFB_n$ and $LRFA_n$ as a function of the number of rows of buildings providing shelter, showing the effect of distance from the shoreline.

3.2.4 Lateral Building Offsets

Rarely in practice does the built environment result in a purely rectangular array of structures. A random placement of buildings reduces the effects of sheltering from the seaward rows. For example, given two rows of buildings, if the second row is offset from the first row in the alongshore direction (perpendicular to the wave direction), then the second row of buildings is directly exposed to wave attack, and would have approximately the same wave loading as the first row.

Defining o as the alongshore offset between centerlines of buildings in adjacent rows, Moris et al. (2021) numerically examined the effects of building offsets. The nondimensional offset, o^* , is defined as the alongshore offset, o , divided by half of the alongshore center-to-center spacing of the

As the building offset increases, wave load reductions decrease, and the wave load becomes essentially the same as the load on row 1.

buildings (half of the gap plus building width). With this definition, an offset that places the second row of buildings in the middle of the gap between the first row of buildings corresponds to $o^* = 1$. Figure 3.2-6 shows numerical results for two tsunami waves. At the far right of the figure, $o^* = 1$, and LRFA is approximately 1.0 for both waves, which means the load is essentially the same as if it were the first row of buildings. For smaller offsets (e.g., $o^* < 0.2$), there is little difference from factors reported for fully sheltered buildings.

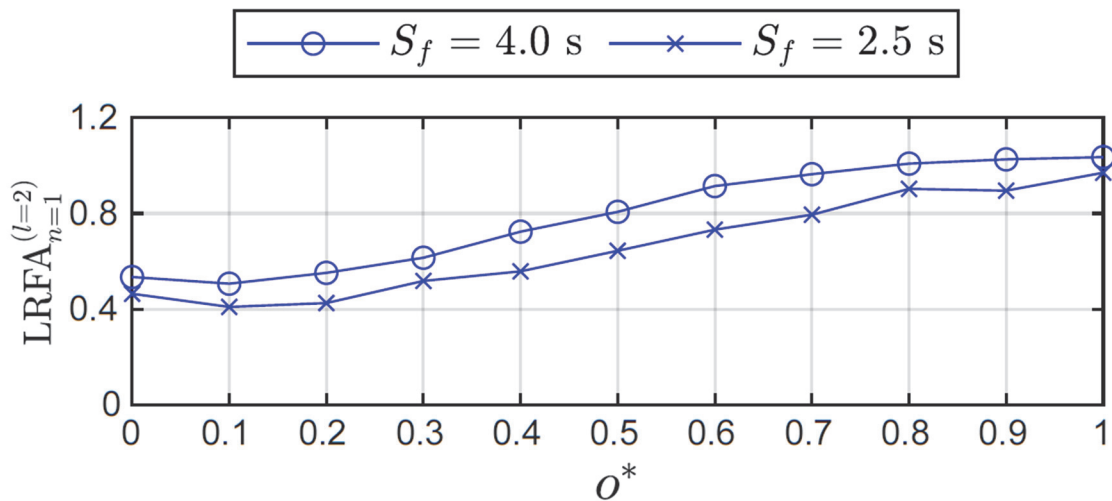


Figure 3.2-6 Plot of $LRFA$ versus nondimensional offset, o^* , showing the effect of building offset on wave loads in row 2.

3.3 Reflected Waves

The reflected wave loads on the back face of buildings in an array can be shown to be much less than the wave loads on the front face of buildings (see Appendix A).

As shown in Figure 3.2-1, waves are observed to reflect from the first row of buildings. They can also reflect from other landward rows in an array, causing loads on the back (landward) face of buildings in the array. The behavior of reflected waves was considered through an analytical extension of the NAS wave transmission coefficient and other knowledge of wave behavior. Using NAS energy concepts, reflected waves on the landward face of buildings can be theoretically calculated. The derivation is described in Appendix A. Based on information presented in the appendix, the reflected energy on the back face of a building is $(1 - r)r$ times the energy on the front face of the building, and the reflected wave loads on the back face of buildings in an array can be shown to be much less than the incident wave load.

3.4 Maximum Inundation Levels, Cross-Shore Velocity, and Cross-Shore Momentum Flux

In this section, differences in maximum inundation levels, cross-shore velocities, and cross-shore momentum flux are discussed for conditions with waves and without waves (i.e., current-only).

3.4.1 Wave Conditions

The maximum free surface elevation with n rows providing shelter is $\eta_{n,\max}$. This quantity is evaluated between structures along the cross-shore centerline (i.e., the center street in the building array perpendicular to the shoreline). Similar to wave load reduction factors, a run-up reduction factor, RRF , can be defined as:

$$RRF = \eta_{n,\max} / \eta_{BE,\max} \quad (3.4-1)$$

Compared to bare-earth conditions, there is a considerable increase in maximum inundation levels in cross-shore streets between buildings due to waves.

where $\eta_{BE,\max}$ is the maximum free surface elevation for bare earth conditions at that location. Rather than a reduction, however, there is a considerable increase in inundation levels in the cross-shore streets (parallel to the direction of flow) due to the presence of the building array, as shown in Figure 3.4-1. When inundation levels in the cross-shore streets between the first row of buildings ($n=0$) are compared to bare earth conditions, the increase in the maximum free surface elevation reaches values up to 2.57 times higher than bare earth free surface elevations.

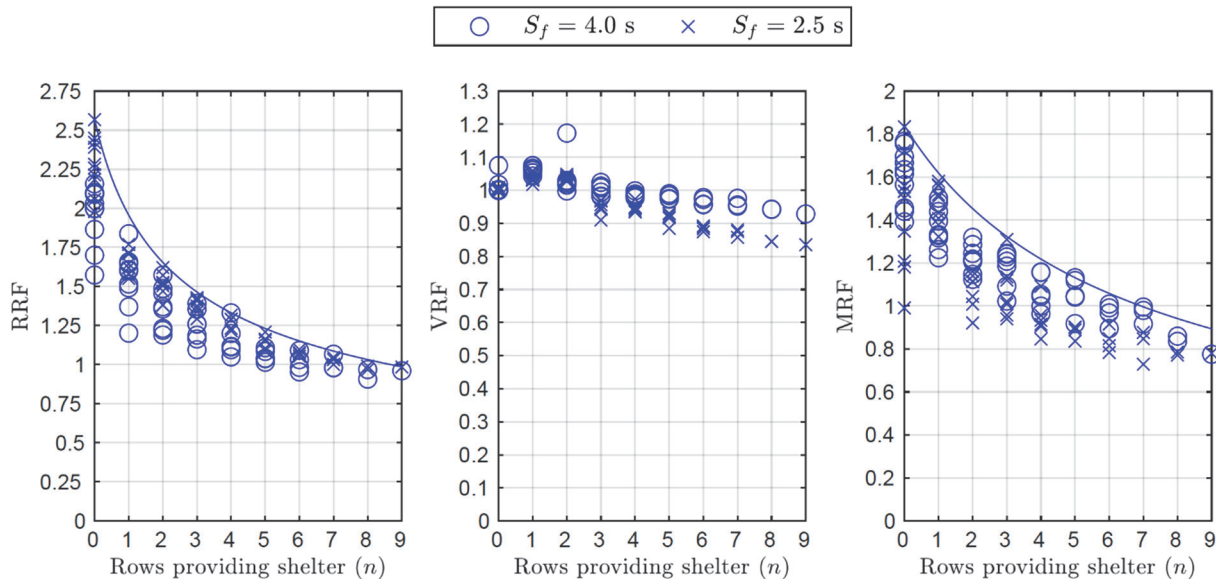


Figure 3.4-1 Numerical run-up reduction factors, RRF , velocity reduction factors, VRF , and momentum flux reduction factors, MRF , as a function of the number of rows providing shelter, n .

The change in maximum cross-shore velocity in the cross-shore streets can be similarly compared to bare earth conditions, as measured by a velocity reduction factor, *VRF*, defined as:

$$VRF = u_{n,\max} / u_{BE,\max} \quad (3.4-2)$$

Compared to bare-earth conditions, overall there is not a large change in maximum horizontal velocities in cross-shore streets between buildings due to waves.

where $u_{n,\max}$ is the maximum horizontal velocity with n rows providing shelter, and $u_{BE,\max}$ is the maximum horizontal cross-shore velocity with bare earth conditions evaluated at the same location where *RRF* is evaluated. As shown in Figure 3.4-1, there is a slight increase in the horizontal velocity in the first rows due to the presence of the building array and a slight decrease of velocity when $n \geq 4$, but, overall, there is not a large change from bare earth maximum horizontal velocities.

Finally, the change in maximum momentum flux in the cross-shore streets can be compared to bare earth conditions, as measured by a momentum flux reduction factor, *MRF*, defined as:

$$MRF = M_{n,\max} / M_{BE,\max} \quad (3.4-3)$$

Compared to bare-earth conditions, there is a noticeable increase in maximum momentum flux in cross-shore streets between buildings due to waves.

where $M_{n,\max}$ is the maximum momentum flux with n rows providing shelter, and $M_{BE,\max}$ is the momentum flux for bare earth conditions. Both quantities are evaluated in the cross-shore streets between structures. As shown in Figure 3.4-1, and similar to results for inundation levels, the presence of a building array led to a noticeable increase of the maximum momentum flux in the cross-shore streets compared to bare earth conditions. Results indicate that critical infrastructure in areas where flow constriction can happen should be carefully analyzed for potential increases in maximum inundation levels and momentum flux due to wave conditions.

3.4.2 Current-Only Conditions

For current-only conditions (i.e., the absence of waves), Figure 3.4-2 plots mean steady-state current velocities measured in the centerline of the cross-shore streets, 0.1m in front of Rows 1-6. Velocities in front of Row 1 (i.e., outside the array) are noticeably lower than velocities within the array, where the flow is channelized in the cross-shore streets.

In current-only conditions, the velocity inside the array can be approximated as $1/r$ times the velocity outside the array

If stillwater depths vary by small amounts, as would be expected for low Froude number flows, it is possible to approximate velocities inside the array based on the velocities just outside the array. In all cases, the total volumetric flow rate through the array must remain constant. For small variations in depth, the velocity inside the array (Rows 2-6) will increase by a factor of approximately $1/r = 1/0.6$ times the velocities outside the array (Row 1). This

theoretical velocity is plotted in Figure 3.4-2 as a dashed line, and is shown to be very close to the mean velocities measured within the array.

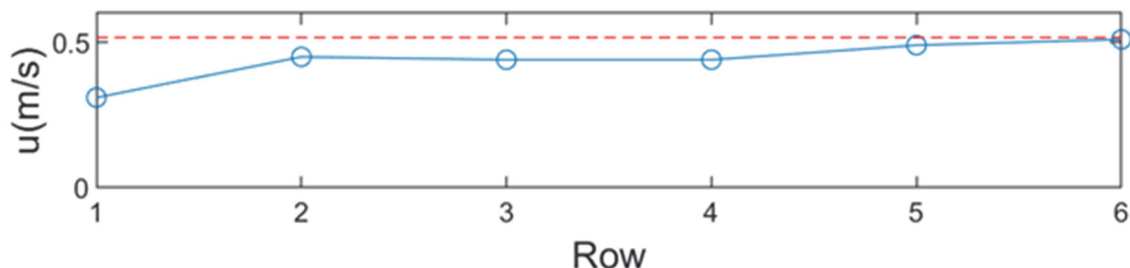


Figure 3.4-2 Mean velocities from current-only experimental tests, measured in the centerline of cross-shore streets (open circles), compared with the velocity just outside the array multiplied by $1/r = 1/0.6$ (dashed line).

Mean stillwater surface elevations were not accurately measured during current-only experimental tests, but results from computational simulations plotted in Figure 3.4-3 show only small changes (i.e., decreases) in surface elevation along the centerline of cross-shore streets at locations 0.1m in front of Rows 1-6, which is consistent with the observed results for mean velocities in current-only conditions.

In current-only conditions, stillwater surface elevations are approximately constant within the array.

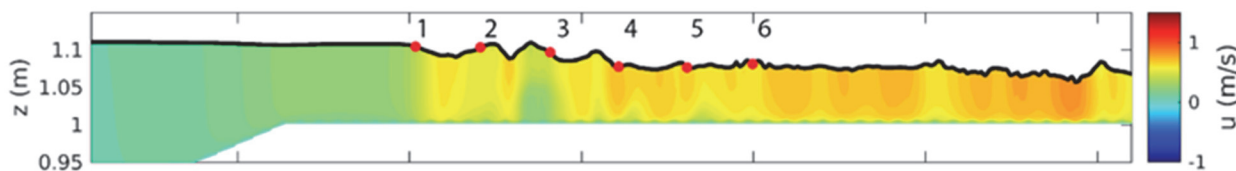


Figure 3.4-3 Computed stillwater surface elevations along the centerline of cross-shore streets (solid line), showing values 0.1m in front of Rows 1-6 (red dots); colors indicate instantaneous velocities for current-only flow.

3.4.3 Effect of Boundary Conditions at the Landward End of a Building Array

The boundary conditions at the landward end of the building array affect the propagation of waves and currents through the array. In the laboratory experiments, waves and currents flowed through the array and drained into a channel, allowing a net flow of fluid through the array. As the tsunami waves were created by the displacement of a paddle, most of the 17.5 m^3 of water that the wave paddle pushed into the tsunami flowed through the building array. This would be representative, for example, of a community on a barrier island or on a coastal plain. However, many communities are backed by a bluff or elevated land, so there can be no net flow through the building array. This would change the nature of the flow through a community (i.e., zero net flow in an upland-backed community), likely resulting in higher

water levels, and changes in maximum cross-shore velocity and cross-shore momentum flux.

3.5 Probability of Debris Impact within an Array

Figure 3.5-1 shows the numbers of collision events (i.e., debris impacting a structure at least once) for each building in an array for both wave-current and current-only conditions.

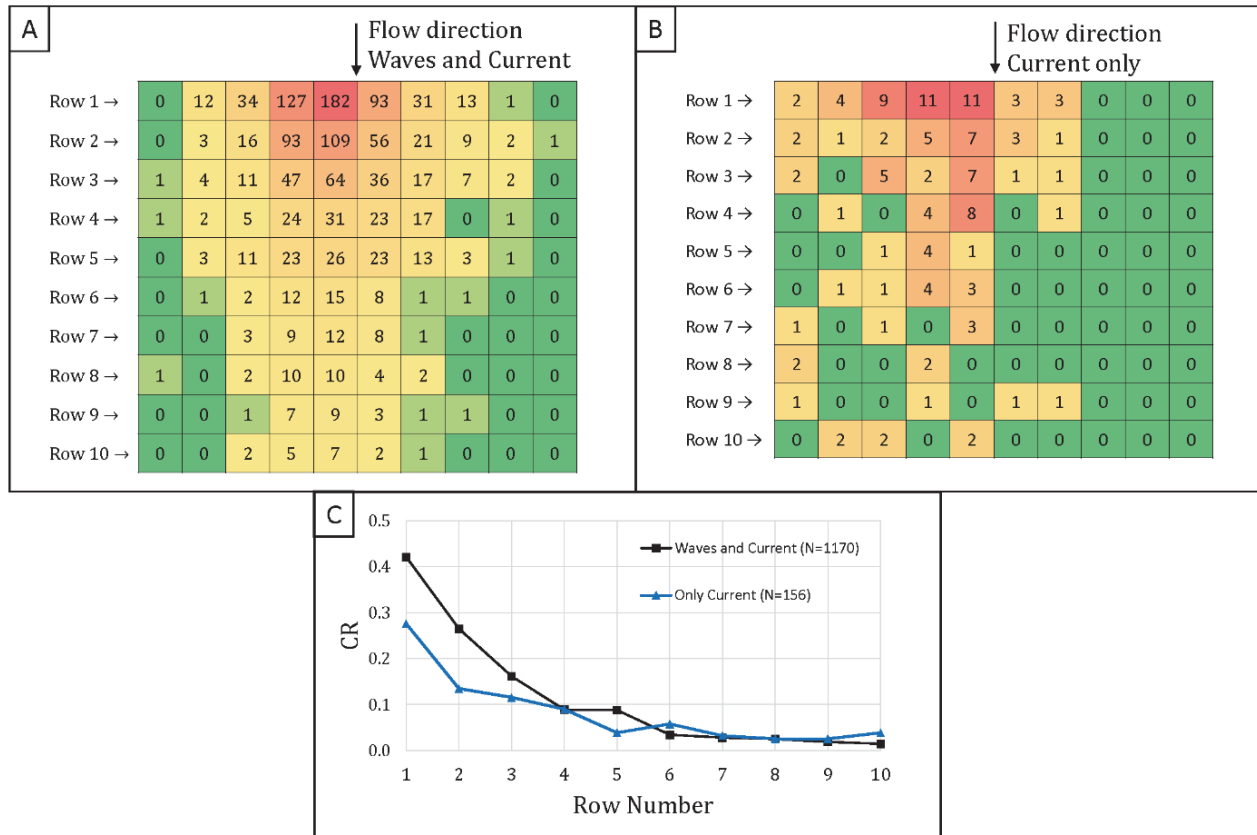


Figure 3.5-1 Results from debris impact experiments: (A) collision map showing the total number of collision events in each building for the wave-current condition, $N_T = 1170$; (B) collision map showing the total number of collision events in each building for the current-only condition, $N_T = 156$; and (C) collision ratio as a function of row number, n .

Although there is a clear central area, with spreading on either side downstream from where the debris were dropped, Figure 3.5-1c shows that overall collisions by row are relevant. The collision ratio, CR , is defined as:

$$CR = \frac{N_{\text{row } n}}{N_T} \quad (3.5-1)$$

where $N_{\text{row } n}$ is the number of collisions by row, and N_T is number of debris events (i.e., number of debris dropped). From the collision map, it becomes clear that the probability of a collision event decreases significantly with

increased sheltering. This is almost certainly because the first row has more frontal area exposed to the flow, and debris can impact anywhere along the front face or corners, while landward rows have much more channelized flow along the cross-shore streets and less opportunity for debris impacting the structures. However, it should be noted that in these experiments, mean flow is aligned with the cross-shore streets, and mean currents at an oblique angle would likely give somewhat different results.

In current-only conditions, debris may be somewhat less likely to impact structures than in wave plus current conditions. This is likely because waves, particularly breaking waves, will transport debris to the front faces of structures, while currents tend to flow around and avoid the front faces of structure, making debris impacts more likely to occur at the corners.

3.6 Variation of Debris Impulse within an Array

For each collision event, the impulse applied by the debris was estimated on all instrumented buildings in the cross-shore direction $I_{0,x}$ and on M-LC-1 in the alongshore direction $I_{0,y}$. It should be noted that absolute values were considered in the alongshore direction because there could be either positive or negative values depending on the angle of impact. These were made dimensionless, $\bar{I}_{0,x}, \bar{I}_{0,y}$, using a representative impulse taking into account both waves and currents at the structure location and differing for each row:

$$\begin{aligned}\bar{I}_{0,x} &= I_{0,x} / p_n \\ \bar{I}_{0,y} &= I_{0,y} / p_n\end{aligned}\quad (3.6-1)$$

where the representative impulse is:

$$p_n = mu + m \frac{H_s}{2h} \sqrt{gh} \quad (3.6-2)$$

where m is mass, u is horizontal velocity, H_s is the significant wave height, h is the stillwater depth, and g is the acceleration of gravity. In the current-only limit, this collapses to the standard steady current impulse, but for wave-current flow, it adds the shallow-water approximation to the orbital velocity of the significant wave height. In this way, it may prove usable for more general conditions.

For debris events with more than one collision, the collision with the largest impulse is considered representative. For debris events with no collision, $I_{0,x}, I_{0,y}$ are taken as 0. For each instrumented building and for each direction, the impulses applied by each debris are sorted in ascending order. This allows the calculation of the probability of exceeding the i^{th} ranked load, P_i :

$$P_i = 1 - \frac{R_i}{N+1} \quad (3.6-3)$$

where N is either the total number of debris events or the number of collision events, and R_i is the ranking of the load, with $R_i = N$ for the largest load measured and $R_i = 1$ for the smallest. Figures 3.6-1 and 3.6-2 show the empirical exceedance probability of the dimensionless impulses for both debris events (including misses) and collision events (only events with recorded collisions).

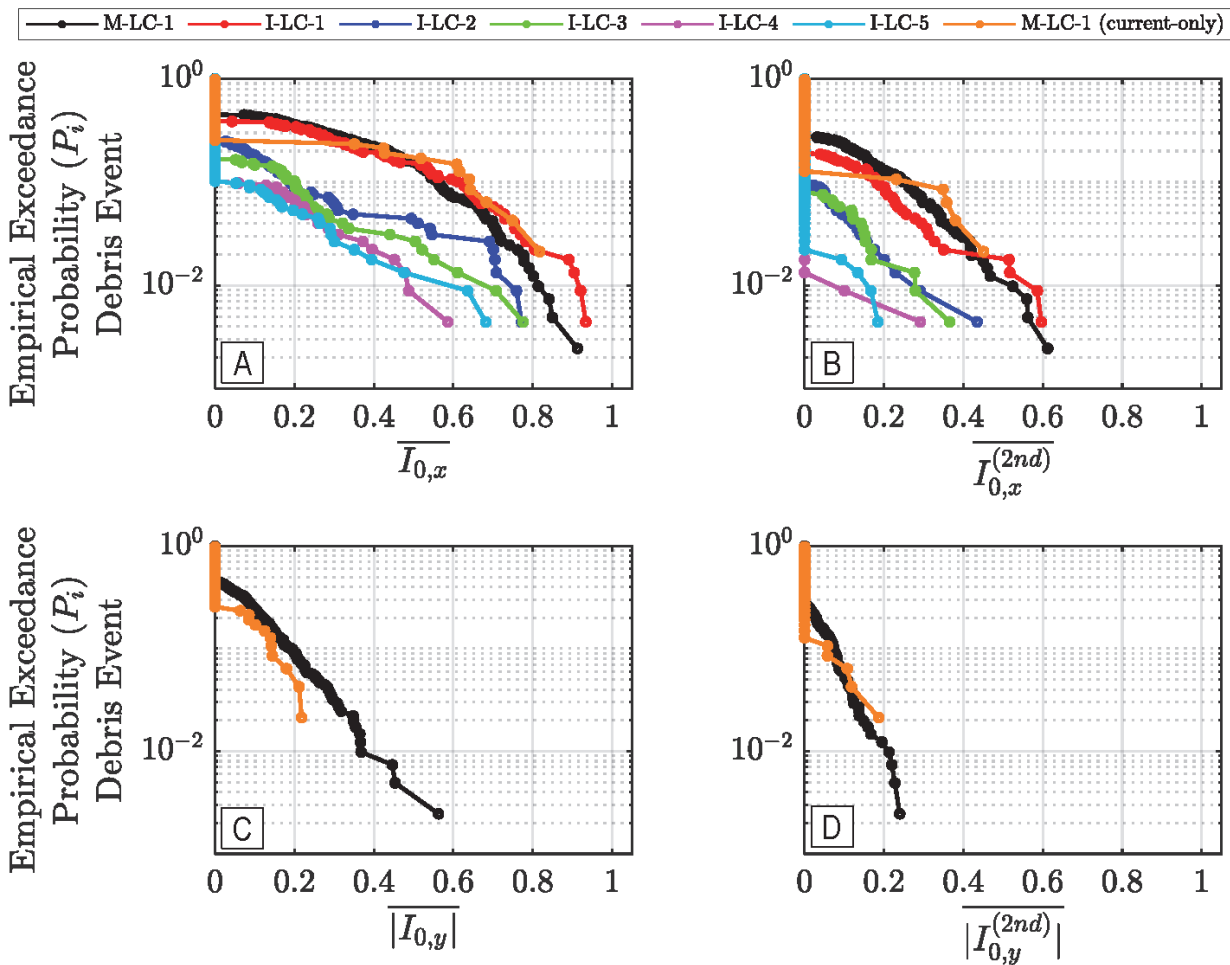


Figure 3.6-1 Empirical exceedance probability within a debris event, x-direction (cross-shore) and y-direction (alongshore), for: (A) the largest applied impulse in the x-direction $\overline{I_{0,x}}$; (B) the second largest applied impulse in the x-direction $\overline{I_{0,x}^{(2nd)}}$; (C) the largest applied impulse in the y-direction $\overline{|I_{0,y}|}$; and (D) the second largest applied impulse in the y-direction $\overline{|I_{0,y}^{(2nd)}|}$ (orange markers indicate a current-only condition).

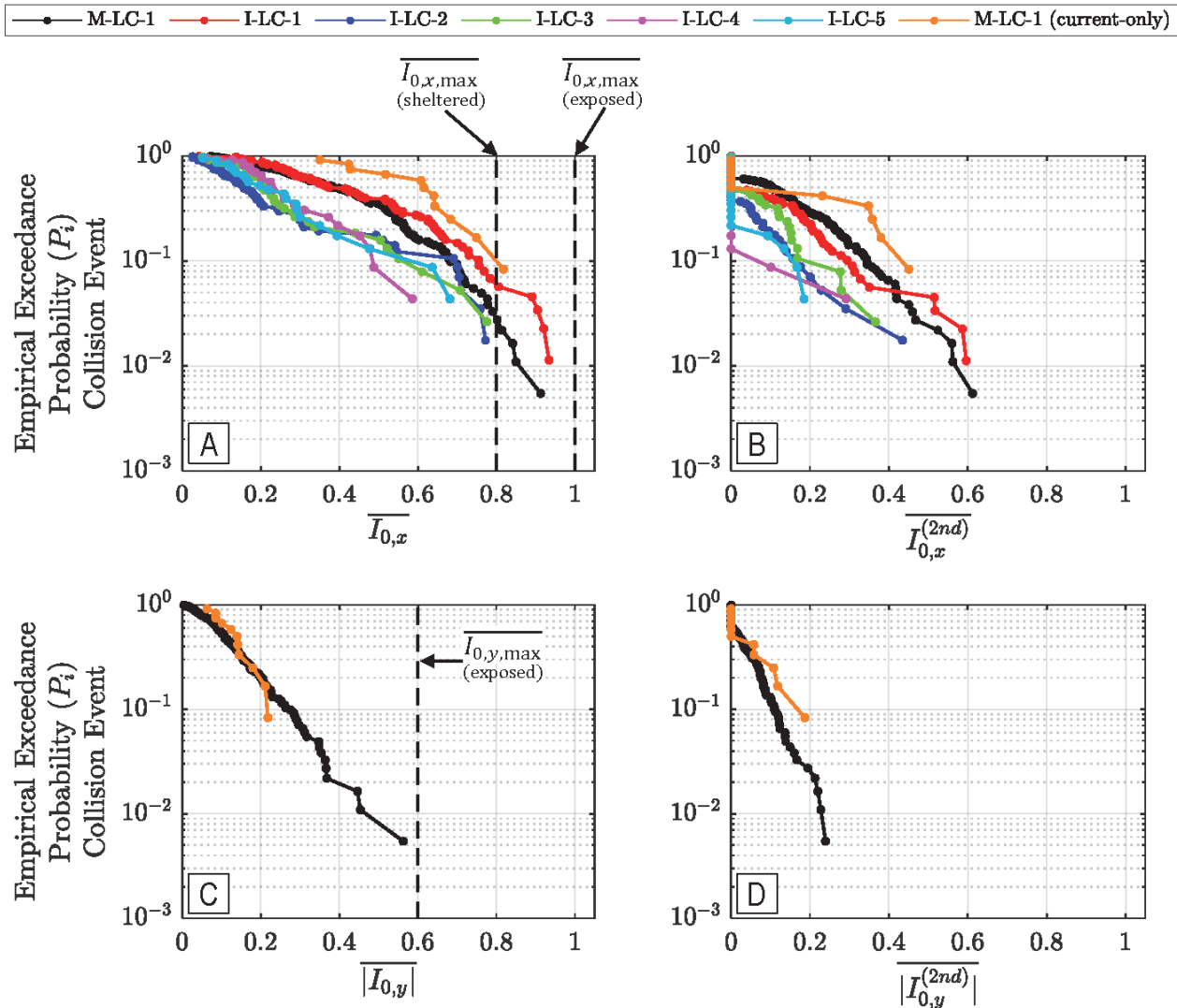


Figure 3.6-2 Empirical exceedance probability within a collision event, x-direction (cross-shore) and y-direction (alongshore), for: (A) the largest applied impulse in the x-direction $\overline{I_{0,x}}$; (B) the second largest applied impulse in the x-direction $\overline{I_{0,x}^{2nd}}$; (C) the largest applied impulse in the y-direction $\overline{I_{0,y}}$; and (D) the second largest applied impulse in the y-direction $\overline{I_{0,y}^{2nd}}$ (orange markers indicate a current-only condition).

In the figures, the hydrodynamic condition corresponds to the wave-current condition, unless otherwise noted (orange markers indicate a current-only condition). The plots show that debris collisions in wave-current and current-only flows are probabilistic in that there is a probability that a collision event will occur as well as the impulse magnitude within the collision event. As such, debris impulse should be described probabilistically, either at a given probability level, or by taking an envelope value. Also, sheltered landward rows not only have lower collision ratios, but also lower dimensionless

impulses as compared to exposed rows. This may be partially explained by the tendency for more glancing collisions on the corners of structures in landward rows as compared to wave-driven collisions on the front face of structures in the first row.

A possibly more surprising result is the large magnitude of impulses, $\bar{I}_{0,y}$, in the alongshore direction (perpendicular to the direction of waves and currents). Alongshore impulses are approximately 60% of the cross-shore impulses, and appear to arise from debris impacting the corner of a structure, or at an oblique angle. Debris loads perpendicular to the direction of waves and currents are not predicted by any standard, but may warrant future consideration.

Based on experimental results, the following values of dimensionless impulse can be considered:

- $\bar{I}_{0,x,\max} = 1.0$ in the cross-shore direction
- $\bar{I}_{0,x,\max} = 0.8$ for sheltered structures
- $\bar{I}_{0,y,\max} = 0.6$ in the alongshore direction

For debris events with multiple collisions (i.e., the same object on the same structure), the second largest collision is not that much smaller than the largest. For example, in the first row of an array, the second largest impulse may be approximately 2/3 of the largest impulse in wave-current flow conditions, as the waves repeatedly drive the debris into the structure.

As possible guidance for engineering design, or inclusion in future standards, approximate limits for maximum dimensionless impulses may be taken from the observed impulse magnitudes. As shown in Figure 3.6-2, values of $\bar{I}_{0,x,\max} = 1.0$ and $\bar{I}_{0,y,\max} = 0.6$ for exposed structures, and $\bar{I}_{0,x,\max} = 0.8$ for sheltered structures, can be considered.

3.7 Maximum Loads from Debris

3.7.1 SDOF Model and Modifications

More complex systems are often simplified as single-degree-of-freedom (SDOF) models. System response can be obtained using Duhamel's integral. For impulsive loading, when $\Delta t / T_n \leq 0.25$, external debris loads on the system may be approximated by an instantaneously applied load using a Dirac delta function $F_x(t) = I_{0,x}\delta(t)$, with $I_{0,x}$ being the impulse applied by the debris in the x-direction. The time-varying load felt by the structural system, $F_{r,x}(t)$, is then:

$$F_{r,x}(t) = I_{0,x} \frac{\omega_n^2}{\omega_d} \exp(-\xi\omega_n t) \sin \omega_d t \quad (3.7-1)$$

where $\omega_n = \sqrt{k/m}$ is the natural frequency of the system, $T_n = 2\pi/\omega_n$, $\xi = c/(2m\omega_n)$ is the damping ratio, and $\omega_d = \omega_n \sqrt{1 - \xi^2}$ is the damped frequency. The maximum load felt by the system is then given by:

$$F_{r,x,\max} = \frac{2\pi}{T_n} I_{0,x} \lambda(\xi) \quad (3.7-2)$$

where:

$$\lambda(\xi) = \exp\left(\frac{-\xi \cos^{-1} \xi}{\sqrt{1-\xi^2}}\right) \quad (3.7-3)$$

using appropriate values of the coefficients. Figure 3.7-1 shows a comparison between Equation 3.7-2, using $I_{0,x}$ measured for each collision event, and the corresponding experimental peak loads.

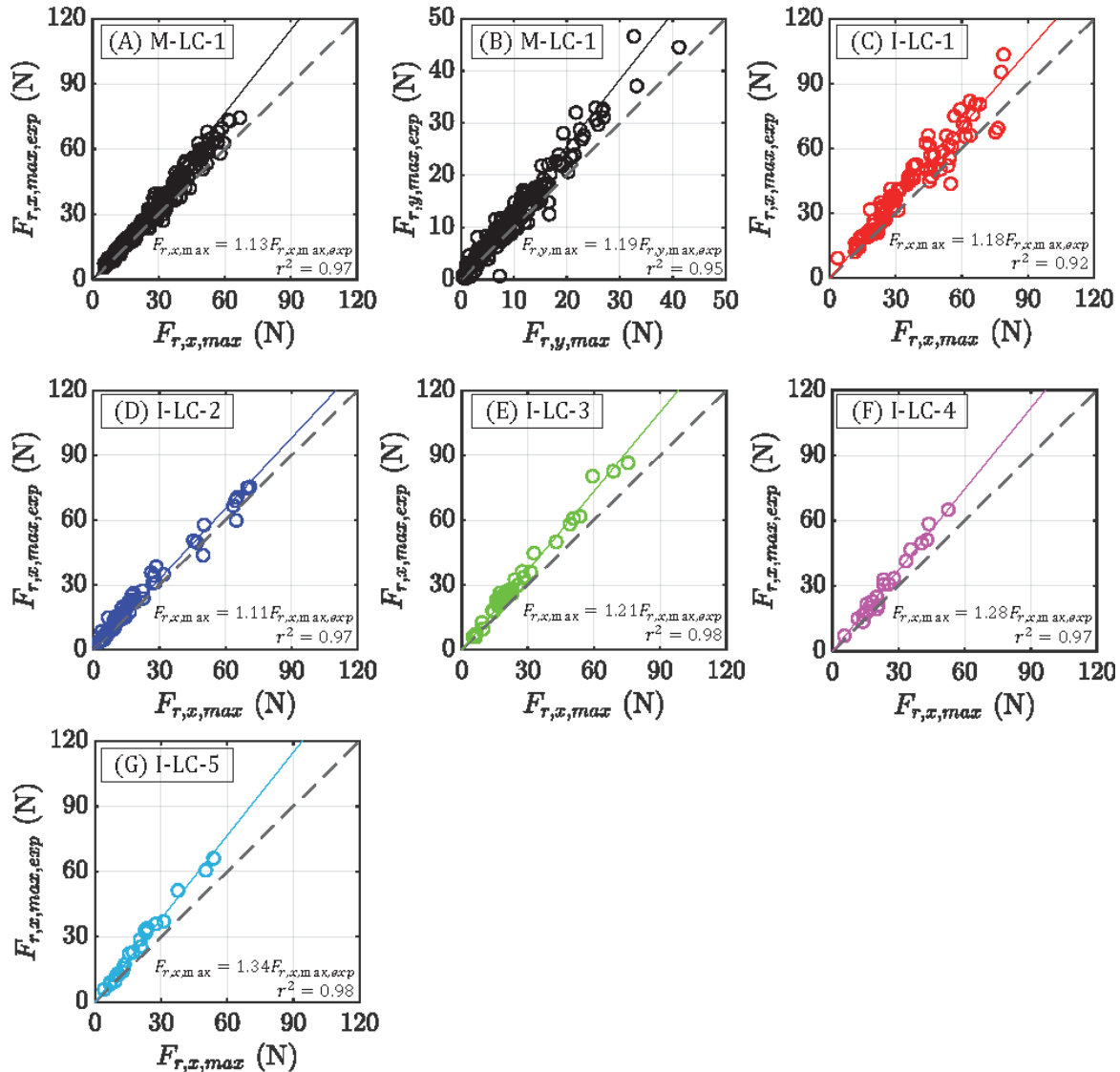


Figure 3.7-1 Comparison of maximum load, x-direction (cross-shore) and y-direction (alongshore), from Equation 3.7-2 and experimental peak loads: (A) M-LC-1, x-direction; (B) M-LC-1, y-direction; (C) I-LC-1, x-direction; (D) I-LC-2, x direction; (E) I-LC-3, x-direction; (F) I-LC-4, x-direction; and (G) I-LC-5, x-direction.

In the figure, solid lines are a best fit to the experimental data, and dashed lines represent a theoretical 1:1 correspondence between experimental data and Equation 3.7-2. Correlation coefficients are extremely high, with $r^2 = 0.92$ to 0.98 , but measured peak loads are consistently 10% to 35% higher than predicted by Equation 3.7-2. Closer inspection of the data shows that, in addition to the fundamental mode, there are also secondary modes with higher frequencies contributing to response. Higher-mode responses tend to increase peak loads above those predicted from a SDOF model, which will be accounted for through the use of an additional factor, $C_s = 1.3$.

With the additional factor, C_s , and substituting Equations 3.6-1 for $I_{0,x}, I_{0,y}$ yields the following equations for maximum predicted cross-shore and alongshore impact loads derived from experimental data:

$$\begin{aligned} F_{r,x,\max} &= \frac{2\pi}{T_n} \bar{I}_{0,x,\max} p_n \lambda(\xi) C_s \\ F_{r,y,\max} &= \frac{2\pi}{T_n} \bar{I}_{0,y,\max} p_n \lambda(\xi) C_s \end{aligned} \quad (3.7-4)$$

3.7.2 Comparison of ASCE 7-22 Flood and Tsunami Loads

Although ASCE 7-22 equations for flood and tsunami debris impact loads look different, there is a close relationship to the impact load equations derived herein.

ASCE 7-22 contains equations for debris loading in the Commentary for Chapter 5 (Flood Loads) and in the Provisions of Chapter 6 (Tsunami Loads). Although the two approaches appear quite different from each other, and from the derivations presented herein, there is a close relationship.

In ASCE 7-22 Chapter 5 Commentary, Equation C5.4-3 gives the debris impact as:

$$F = \frac{\pi W V_b C_I C_O C_D C_B R_{\max}}{2g \Delta t} \quad (3.7-5)$$

where F is the impact load, $W = mg$ is the debris weight, V_b is the object velocity, g is gravity, and Δt is the duration of impact. There are then several coefficients: C_I is an importance coefficient, $C_O = 0.8$ is an orientation coefficient, C_D is a depth coefficient, C_B is a blockage coefficient, and R_{\max} is a dynamic response ratio. The commentary notes that with the coefficients set equal to 1.0, the equation reduces to $F = \pi W V_b / 2g \Delta t$, which seems to indicate that the magnitude of the load increases as the duration of impact decreases. The problem with this narrative is that it is both wrong and misleading. This is because the factor, R_{\max} , hides a systematic variation that changes the way the equation is interpreted. If the fundamental natural period of the structural component under consideration is T_n , and $C_{R\max}$ is defined as $C_{R\max} = R_{\max} (\Delta t / T_n)^{-1}$, the debris impact load can then be written as:

$$F = \frac{\pi m V_b C_I C_O C_D C_B C_{R\max}}{2T_n} = \frac{\pi I_0 C_I C_O C_D C_B C_{R\max}}{2T_n} \quad (3.7-6)$$

For $\Delta t / T_n \leq 0.2$ (impulsive loading), clear upstream conditions, Risk Category II importance, and depths greater than 5 feet, $C_{R\max} = 4$, $C_I = C_D = C_B = 1.0$, and the equation may be further simplified to

$$F = \frac{1.6\pi I_0}{T_n} \quad (3.7-7)$$

which is closely related to Equation 3.7-2, but with slightly different coefficients, and without the influence of structural damping. This form is significantly different from the ASCE 7-22 equations, but much better represents the actual processes in that load is a function of debris impulse and fundamental structural period. For lightly damped structures, ASCE 7-22 equations will always give smaller loads than experimental results presented herein.

Table 3.7-1 Dynamic Response Coefficients, R_{\max} from ASCE 7-22, Recast as $C_{R\max}$

| $\Delta t / T_n$ | R_{\max} | $C_{R\max} = R_{\max} (\Delta t / T_n)^{-1}$ |
|------------------|------------|--|
| 0.0 | 0.0 | 4.0 |
| 0.1 | 0.4 | 4.0 |
| 0.2 | 0.8 | 4.0 |
| 0.3 | 1.1 | 3.667 |
| 0.4 | 1.4 | 3.50 |
| 0.5 | 1.5 | 3.0 |
| 0.6 | 1.7 | 2.833 |
| 0.7 | 1.8 | 2.571 |
| 0.8 | 1.8 | 2.25 |
| 0.9 | 1.8 | 2.0 |
| 1.0 | 1.7 | 1.7 |
| 1.1 | 1.7 | 1.546 |
| 1.2 | 1.6 | 1.333 |
| 1.3 | 1.6 | 1.231 |
| ≥ 1.4 | 1.5 | $2.1 (\Delta t / T_n)^{-1}$ |

A similar situation occurs with tsunami loads. In ASCE 7-22, Chapter 6 Provisions, the design instantaneous debris impact load is defined as:

$$F_i = I_{tsu} C_O F_{ni} \quad (3.7-8)$$

where I_{tsu} is an importance factor, C_O is an orientation coefficient equal to 0.65 for logs and poles, and F_{ni} is the nominal maximum instantaneous debris impact load. For an equivalent elastic static analysis, the impact load is multiplied by the dynamic response ratio, R_{max} , as shown in Table 3.7-1, above. The impulse duration is computed as:

$$\Delta t = \frac{2mu_{\max}}{F_{ni}} \quad (3.7-9)$$

where m is the mass of the debris (W/g), and u_{\max} is the maximum flow velocity at the site occurring at a depth sufficient to float the debris. For Risk Category II importance and $\Delta t / T_n \leq 0.2$, a procedure similar that used for flood loads yields:

$$F = \frac{5.2I_0}{T_n} \quad (3.7-10)$$

which is, again, closely related to Equation 3.7-2, and significantly different from the form of equations in ASCE 7-22.

Table 3.7-2 compares three forms of the maximum impulsive debris load equation (from ASCE 7-22 Flood, ASCE 7-22 Tsunami, and Equation 3.7-4 derived from experimental results herein), for Risk Category II importance, deep, unobstructed flow, $I_0 = p_n$, and zero damping.

Table 3.7-2 Comparison of Maximum Impulsive Debris Load Equations, in the Direction of Waves and Current Flow, for First Row Structures, Risk Category II Importance, Deep Unobstructed Flow, and Zero Damping

| Source | <i>Simplified Equation for Impulsive Loading, Typical Coefficients, Undamped Structure</i> |
|---|--|
| Derived from ASCE 7-22 Flood | $F = 1.6\pi p_n / T_n \approx 5.03 p_n / T_n$ |
| Derived from ASCE 7-22 Tsunami | $F = 5.2 p_n / T_n$ |
| Derived from experimental data (Equation 3.7-4) | $F = 2\pi p_n C_s / T_n \approx 8.17 p_n / T_n$ |

For the conditions noted, the three equations appear to be identical in form, but with somewhat different coefficients. As suggested by experimental results, the present derivation (Equation 3.7-4) yields the largest loads. In the more general case, as damping and other factors become more significant, the equations may result in larger differences, but the general trends are expected to hold.

Simplifying coefficients, and synthesizing results to include all load durations using $C_{R\max}$ and to include consideration of damping, the maximum impulsive debris load in the x-direction can be expressed as:

$$F_{r,x,\max} = \frac{2C_{R\max}}{T_n} \bar{I}_{0,x,\max} p_n \lambda(\xi) \quad (3.7-11)$$

The dimensionless impulse given in Section 3.6 for exposed locations is $\bar{I}_{0,x,\max} = 1.0$. With $C_{R\max} = 4.0$ from Table 3.7-1, the combined coefficient $2C_{R\max} \bar{I}_{0,x,\max}$ in Equation 3.7-11 becomes 8.0 for unsheltered structures in the direction of flow, which is nearly identical to the combined coefficient of 8.17 shown for Equation 3.7-4 in Table 3.7-2.

The synthesis could be extended to y-direction loads to yield:

$$F_{r,y,\max} = \frac{2C_{R\max}}{T_n} \bar{I}_{0,y,\max} p_n \lambda(\xi) \quad (3.7-12)$$

Using $\bar{I}_{0,y,\max} = 0.6$ for alongshore impulses, as given in Section 3.6, and $C_{R\max} = 4.0$ from Table 3.7-1, the combined coefficient in Equation 3.7-12 becomes 4.8 for unsheltered structures perpendicular to the direction of flow.

Figure 3.7-2 shows a plot of experimental data for maximum debris impact versus exceedance probability for loads on a row 1 (unsheltered), lightly damped structure (I-LC-1). For comparison, the figure also shows the value from Equation 3.7-7 (adapted from ASCE 7-22 Chapter 5 for flood loads) and the value from proposed Equation 3.7-11, which uses $C_{R\max}$. Because the value from Equation 3.7-10 (adapted from ASCE 7-22 Chapter 6 for tsunami loads) is nearly the same as for flood loads, only ASCE 7-22 flood loads are shown for comparison in the figure.

In the figure, experimental data to the right of the line for ASCE 7-22 indicate that ASCE 7-22 equations for flood (and tsunami) loads are unconservative at the plotted exceedance probabilities. In contrast, it can be seen that the line for proposed equation 3.7-11 conservatively envelopes all experimental data at all exceedance probabilities. For this reason, use of Equations 3.7-11 and 3.7-12 is recommended for debris impact loads on main structural systems in waves and currents.

Figure 3.7-2 shows that ASCE 7-22 equations for flood and tsunami debris impact loads are unconservative relative to experimental results at some exceedance probabilities.

Equation 3.7-11 conservatively envelopes experimental data and is recommended for improved safety and transparency.

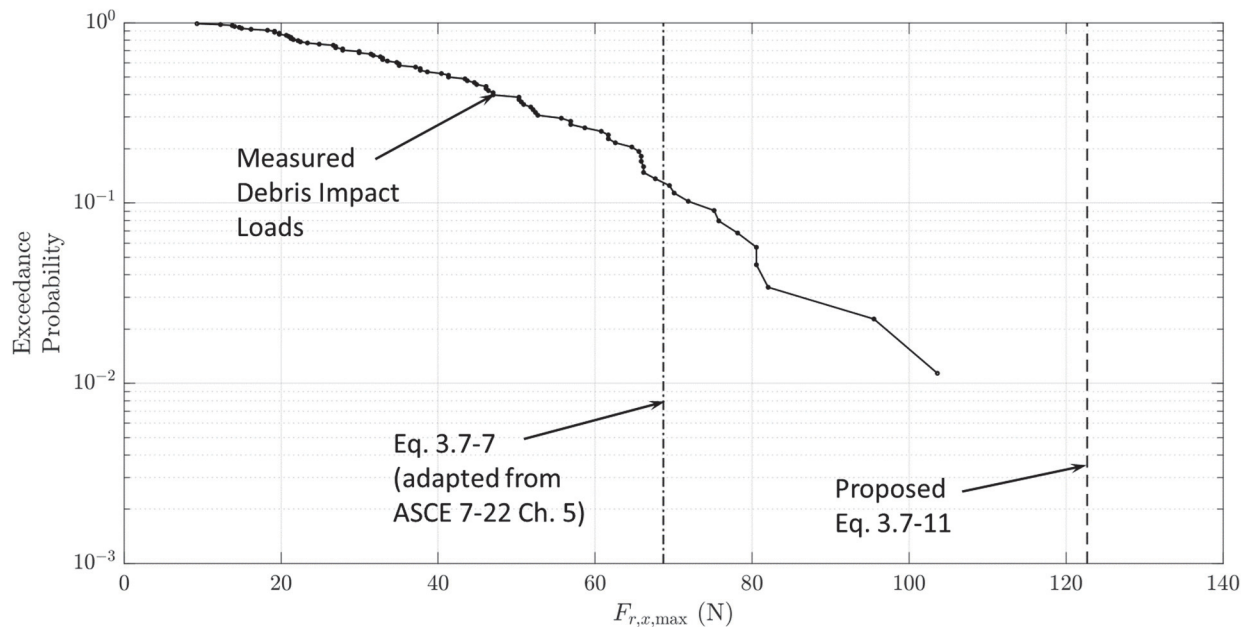


Figure 3.7-2. Plot of maximum experimental debris impact loads versus exceedance probability for a row 1 (unsheltered) structure, compared with the value from Equation 3.7-7 (adapted from ASCE 7-22 Chapter 5 for flood loads) and the value from proposed Equation 3.7-11, with $I_0 = p_n$, $C_I = 1$, $C_B = 1$, and $C_D = 1$.

With the exception of the load orientation coefficient C_O (equal to 0.8 for flood loads and 0.65 for tsunami loads), which is already included, proposed Equations 3.7-11 and 3.7-12 can be adapted to incorporate additional ASCE 7-22 coefficients. Importance factors (C_I for flood loads and I_{tsu} for tsunami loads) can be applied directly, as can the flood load blockage coefficient, C_B , and depth coefficient, C_D .

Chapter 4

Recommendations

This chapter recommends improvements to building design practice related to coastal flooding within developed areas, and to flood provisions in codes and standards. It outlines how results can be used: (1) by designers to shift design practice from a *Simplified Approach* to an *Enhanced Approach* (described in Section 1.2) for estimating flood hazards within a building array; and (2) by code committees as the basis for future proposals to improve floodborne debris impact load calculations in Chapters 5 and 6 of ASCE 7.

4.1 Improvements to Present Design Practice

When faced with designing a building to resist flood loads, many designers make simple and conservative estimates of flood hazards (i.e., flow depth, velocity, and direction; wave height and direction; and floodborne debris type, weight, velocity, and direction). This often means the most hazardous flow, waves, and debris able to reach *any* submerged portion of *any* nearby building from *any* direction, and are assumed to reach *all* submerged portions of the building of interest from *all* directions. This *Simplified Approach* is very conservative, especially when the building is situated within an array of buildings, where streets and neighboring buildings can alter the flow and wave fields, sheltering some buildings, and focusing the loads on others. Recommendations are intended to help designers move toward an *Enhanced Approach*, where knowledge about flood propagation within building arrays can be used to improve estimates of flow and wave directions, flow velocities, local wave heights, and likely debris impacts.

Laboratory and numerical experiments were performed using a 10×10 or 10×3 regular building array (see Figure 1.1-1) with a level ground surface. Thus, most of the results pertain to a regular array. However, some experiments were run using an array with offset buildings, as shown in Figure 4.1-1. In these experiments, building offsets occurred in row 2. The figure shows offsets occurring in row 3. In actual developed regions, building offsets could occur in any row, and offset experiments can be used to extend regular array results to more realistic cases occurring in developed regions. The sections that follow make recommendations on present design practice for regular and irregular array scenarios.

The *Simplified Approach* is very conservative, especially when a building is situated within an array of buildings.

Recommendations are intended to help designers move toward an *Enhanced Approach*, where knowledge about flood propagation within an array can be used to improve estimates of flow and wave directions, flow velocities, local wave heights, and likely debris impacts

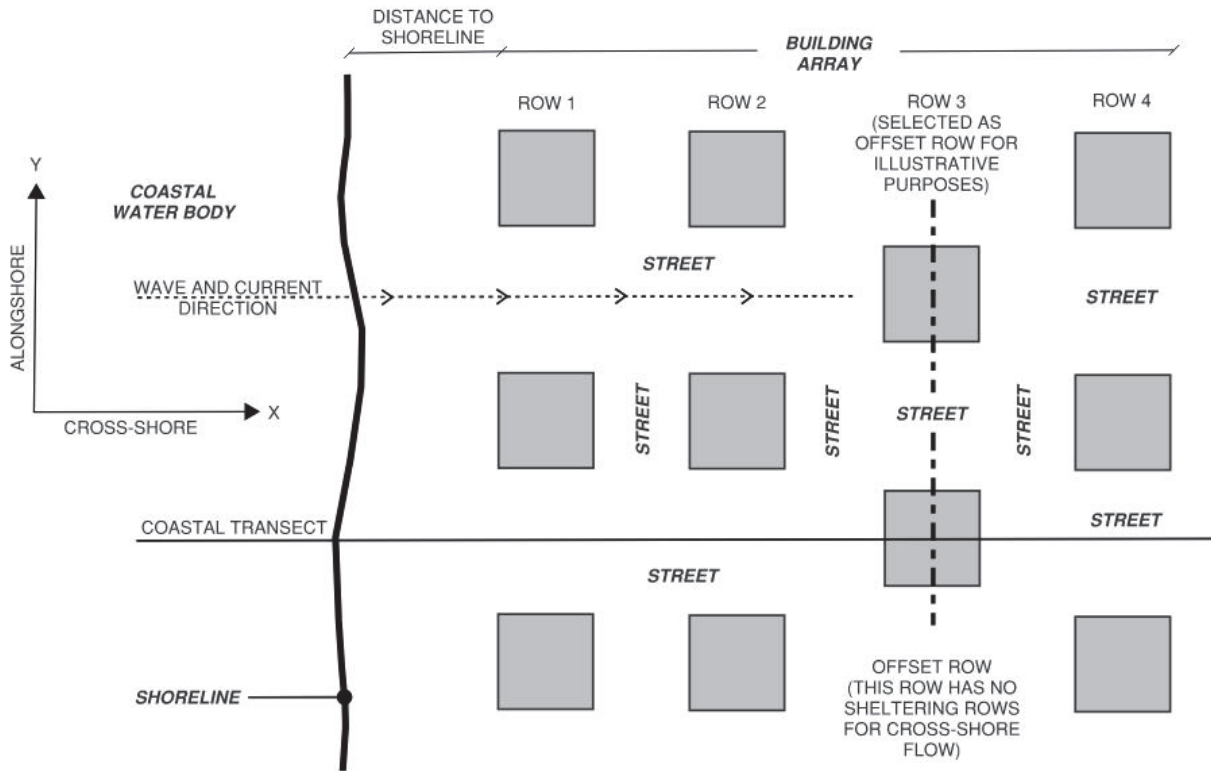


Figure 4.1-1 Plan view showing offset buildings in a simplified building array (as compared to Figure 1.1-1).

It is noted that laboratory and numerical experiments were run with waves and currents perpendicular to the shoreline and the rows of buildings. Waves and currents approaching at an oblique angle to an array might affect some of the findings and recommendations provided herein, and could result in some wave and debris loads on the cross-shore faces of buildings.

4.2 Flow Depths and Velocities

The stillwater flood surface is approximately level throughout a regular array, and the stillwater flow depths tend to be approximately uniform over horizontal ground.

The total water surface elevation can vary due to the presence of waves (i.e., due to passage of overland waves and wave runup against buildings), but when wave effects are removed, laboratory and numerical results show that the stillwater flood surface is approximately level throughout a regular array, and the stillwater flow depths throughout a regular array with constant ground elevation tend to be approximately uniform. One exception to this is the scenario where the downstream water level (e.g., in a bay behind a barrier island) is lower, which leads to a drop in the water level in the downstream portion of the array. However, the bay is likely to fill during a design level flood event, and this downstream lowering is likely to be short-lived.

This suggests that designers can assume the stillwater surface within the array is approximately level for design purposes. Stillwater flood depths,

therefore, can be assumed to vary only with the ground elevation throughout the array. As the ground rises the flood depth will decrease, and as the ground falls the flood depth will increase.

With the flood level approximately constant, flows through an array are controlled by the layout of the streets in the array, the blockage effects of buildings, and the direction of the incident current across the shoreline and towards the array. Flow will tend to follow the streets as it moves around the buildings. In a regular array with incident currents perpendicular to the shoreline, flow will move around the first-row buildings and be “channeled” along the cross-shore streets between the buildings such that there is little flow in the alongshore streets beyond the first row³. In an offset array, flow will be channeled in the cross-shore streets until the flow encounters offset buildings that are partially blocking the channels, at which point the flow will be redirected in the alongshore streets around the offset buildings, until it finds its way back into cross-shore streets between buildings.

Flow velocities within the cross-shore channels of a building array will be greater than the flow velocities across the shoreline in the corresponding bare earth condition. This is because the buildings in the array block part of the area through which the cross-shore flow would otherwise pass. Using the same convention as NAS (1977) for wave dissipation (section 3.1), where the fraction of open space through which flow passes is the gap ratio, r , the fraction of area blocked is the blockage ratio, w^* , and r and w^* are related by the expression $r = 1 - w^*$, the average velocity in the cross-shore streets of the array will be approximately $1/r$ or $1/(1 - w^*)$ times the velocity in the absence of the buildings (i.e., the bare earth condition)⁴. If a designer can obtain a bare earth velocity from a flood hazard study or otherwise estimate the bare earth velocity at the location of interest, the velocity in nearby cross-shore streets can be approximated using this relationship.

If a bare earth velocity is available from a flood hazard study or other estimate at the location of interest, the velocity in nearby cross-shore streets can be approximated as $1/r$ or $1/(1 - w^*)$ times the velocity in the absence of the buildings.

4.3 Wave Loads

Laboratory and numerical experiments were run with waves only and with waves plus current, and loads on buildings in the array were measured or calculated. Experiments considered long-period, tsunami-like waves with wave fronts parallel to the first row of buildings in the array. Although results are based on tsunami-like waves, they are expected to approximate the behavior of storm waves within an array. Selected results from laboratory

³ Experiments were run with a current direction perpendicular to the shoreline and the building rows, but an oblique angle of approach would be expected to induce alongshore currents in the seaward portion of the array.

⁴ Both r and w^* will have values between 0 and 1, and the sum of r and w^* will be 1.

and numerical studies on wave loads can be integrated into the *Enhanced Approach* for estimating flood hazards as described in the sections that follow.

4.3.1 Variation of Wave Loads within an Array

In general, wave loads diminish in the landward direction as the number of rows of seaward buildings increases. Wave loads on the front row of an array will be the highest, and each row tends to diminish wave energy by sheltering buildings in landward rows.

In general, wave loads diminish in the landward direction as the number of rows of seaward buildings increases. Wave loads on the front row of an array will be the highest, and each row tends to diminish wave energy by sheltering buildings in landward rows (see Section 3.1).

Other parameters (e.g., alongshore spacing, cross-shore spacing, and distance from shoreline to location of interest) can also affect wave dissipation and the resulting wave load reduction (see Section 3.2). The gap ratio, r , is a function of the alongshore spacing of buildings. As the gap ratio decreased, the blockage increased, and wave load reductions were observed to increase. The cross-shore spacing of buildings was observed to influence the beneficial blocking effect provided by seaward rows of buildings. As the cross-shore spacing of rows increased, the blocking effect decreased, and wave load reductions were observed to decrease. Finally, as the distance from the shoreline increased, wave heights and wave loads were shown to diminish.

When the alongshore spacing is irregular, buildings are offset into the gaps between buildings in adjacent rows (see Figure 4.1-1). In such cases, the effect of sheltering from seaward rows is reduced, and wave loads on the faces of buildings in the gaps will be higher than at the faces of nearby buildings that are sheltered (see Section 3.2.4). On offset buildings, experimental results show that the load is essentially the same as if the buildings were unsheltered. On sheltered buildings, the wave energy may be lowest at the center of the front face, and highest near the front corners. In the case of partially sheltered buildings, however, designers should use judgement in determining how wave loads might vary in the alongshore direction. As a simplifying assumption, where buildings are offset due to irregular spacing in the alongshore direction, designers may wish to assume that wave loads on row 1 also apply to row 2 buildings (and possibly to additional landward rows, depending on the actual building layout).

Where buildings are offset due to irregular spacing in the alongshore direction, designers may assume that wave loads on row 1 also apply to row 2 buildings (and possibly to additional landward rows).

4.3.2 Wave Load Reduction Factors

Wave energy and wave loads can be approximated as a function of the square of the wave height. Experimental wave loads in the first 4 to 5 rows of a regular array were observed to diminish in a manner consistent with the NAS (1977) wave height reduction (see Section 3.1). As a result, wave load

reduction factors can be developed based on the number of seaward rows providing shelter and the ratio of open space between buildings.

Although other parameters (e.g., distance from shoreline to location of interest, and cross-shore row spacing) can also affect wave dissipation and the resulting wave load reduction, as a first approximation, these effects will be relatively small in an urban environment and could be neglected for building design purposes. As a simplifying assumption, designers can first determine the wave load on row 1 (e.g., using procedures in ASCE 7-22, Chapter 5) and then apply an appropriate wave load reduction factor, LRF , as indicated in Figure 3.1-3. Theoretically derived values of LRF shown in Figure 3.1-3 should not be taken less than the values shown for $n = 4$, until experimental studies of additional geometries determine that additional conservatism is not warranted in cases with additional rows of sheltering.

Designers can first determine the wave load on row 1 (e.g., using procedures in ASCE 7-22, Chapter 5) and then apply an appropriate wave load reduction factor, LRF , as indicated in Figure 3.1-3.

4.3.3 Reflected Waves

Waves can reflect from landward rows of buildings within an array, causing loads on the back (landward) faces of buildings in the array. Reflected waves in an array can be very complex, arriving at different times, sometimes adding, sometimes cancelling other reflected waves. An analytical extension of NAS energy concepts (see Appendix A) can be used to show that the reflected energy on the back face of a building is $(1 - r)r$ times the energy on the front face of the building.

Relative wave heights, H/H_i , for reflected waves on the landward face of buildings are shown in Figure A.1-1, assuming zero energy dissipation, among other simplifying assumptions. Because wave loads are proportional to the square of wave height, information in Figure A.1-1 can be used to show that the maximum reflected wave load would be 0.25 times the incident wave load and would occur on the back face of row 1, and that reflected wave loads on the back face of subsequent landward rows would be less than 10% of the incident wave load on row 1.

Based on information in Figure A.1-1, the maximum reflected wave load would be 0.25 times the incident wave load and would occur on the back face of row 1, and reflected wave loads on the back face of subsequent landward rows would be less than 10% of the incident wave load on row 1.

4.4 Debris Impact in Wave and Current Conditions

There are several things that designers should consider in estimating debris impact loads:

- Type, size, and mass of floodborne debris objects in the general area
- Incident flow velocity and wave conditions
- Flood depths and channel widths/geometries that limit or affect the ability of debris objects in the area to reach a building of interest

- Building array and street layout, and resulting local flow field (velocity and direction) that can transport debris objects toward a building of interest
- Likelihood and location of debris impacts on a building of interest
- Stiffness of debris object and building element being struck
- Debris impact load equation

Laboratory and numerical experiments addressed some of these factors, including the building array and street layout, the likelihood and location of impacts, and the form of the debris impact load equation. Experiments considered a regular array subjected to cross-shore current and waves in a direction perpendicular to the shoreline and building rows, investigated the likelihood of debris strikes by location within the array, and determined how debris impact loads varied by building row.

4.4.1 Likelihood of Debris Impact

Debris impacts were most common on the front face of buildings in row 1, and near the corners of buildings in landward rows. Results from debris impact studies can be extrapolated to make general predictions of expected behavior of debris transport within an array.

In laboratory experiments, debris objects were observed to be transported by currents through the array. Debris impacts were most common on the front face of buildings in row 1, and near the corners of buildings in landward rows, as shown in Figure 4.4-1. These observations were used to create the collision maps in Figure 3.5-1, which can be used to help inform the estimated likelihood of debris impacts and locations in idealized conditions, although observed results may or may not be representative of more complex situations.

Debris impacts in irregular arrays, or in cases where waves and currents approach the shoreline at an oblique angle, were not tested experimentally, but results can be extrapolated to make general predictions of expected behavior:

- Where waves and currents approach the shoreline at an oblique angle, it is expected that currents will tend to follow the cross-shore and alongshore streets through the array, while waves will tend to propagate principally in the landward direction. As a result, debris impacts on the sides of buildings in row 1 are expected to occur, likely decreasing in landward rows further into the array. Alongshore flow between seaward rows of the array would be expected to result in glancing impacts along the front (seaward) or rear (landward) faces of buildings. Corner impacts would be expected to occur wherever flow is directed towards a corner.

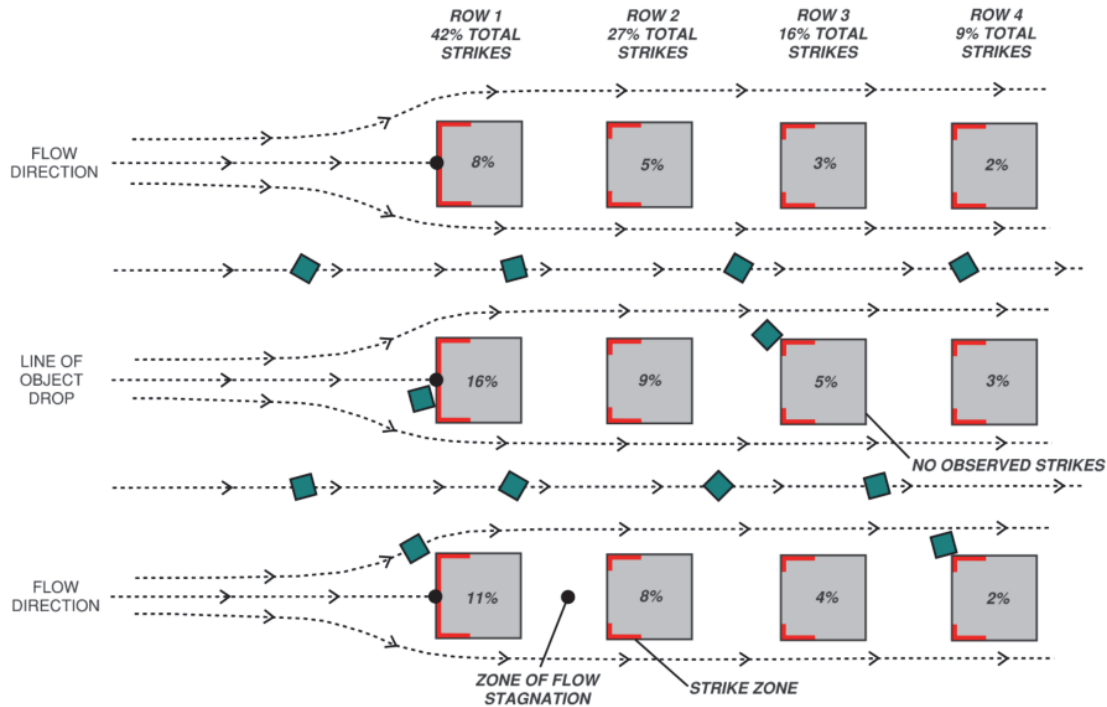


Figure 4.4-1 Plan view showing the location of typical debris impacts throughout the building array.

- In irregular building arrays, debris will impact the seaward faces of buildings in row 1, as well as the seaward faces of landward buildings located in the gaps between row 1 buildings (i.e., building faces that are exposed directly to waves and current passing between row 1 buildings).
- In irregular building arrays with waves and currents approaching the shoreline at an oblique angle, the resulting flow field along the seaward face of row 1, and some landward rows near the front of the array, will have an alongshore component. Currents will tend to follow the cross-shore and alongshore streets through the array, and waves will tend to propagate in the landward direction, however, the flow field will likely be more complex than in the case of a regular array, and rapid changes in flow direction may lead to more debris impacts in landward rows. Corner impacts would be expected to occur wherever flow is directed towards a corner.

Overall, the following trends are expected to occur, and these can be used by designers to better estimate the likelihood and potential locations of debris strikes:

- The front faces of row 1 buildings (all arrays and incident current and wave conditions) will experience the greatest likelihood of debris impact and the highest impact loads.

Experimental trends can be used by designers to better estimate the likelihood and potential locations of debris strikes within an array.

- In an irregular array (all incident current and wave conditions), the exposed faces of landward buildings in gaps between row 1 buildings will experience a likelihood of debris impact and magnitude of impact load that are similar to, and can be somewhat greater than, row 1 buildings.
- The likelihood of debris impacts is expected to diminish in the landward rows of any building array.
- Corner impacts (all arrays and incident current and wave conditions) can occur wherever flows are directed toward a corner.
- Debris strikes on the front face of a building will generate loads perpendicular to the face and loads parallel to the face of the building. Loads parallel to the face of the building can have magnitudes on the order of 60% of the loads perpendicular to the face.
- Side impacts are less common than front face or corner impacts and are likely to have lower impact magnitudes.
- Obliquely incident waves and currents can cause alongshore (lateral) flows, especially between the seaward rows of buildings, and glancing debris impacts can occur on buildings adjacent to these lateral flows.
- Debris transport and potential impact during outflow through an array (i.e., the receding part of a storm hydrograph) should also be considered.

4.4.2 Debris Impact Loads

Impact load equations in ASCE 7-22, Chapters 5 and 6 were shown to be unconservative for stiff structural elements of buildings.

An alternative impact load formulation is recommended in Equation 3.7-11 for improved safety and more transparent recognition of parameters that influence the magnitude of impact loads.

In laboratory experiments, debris impact loads were measured at selected locations within a regular building array. Impact load equations in ASCE 7-22, Chapters 5 and 6 were compared with equations derived in Section 3.7.2, as shown in Table 3.7-2. Experimental measurements, combined with a re-examination of debris impact loading physics, suggest that the impact load equations in ASCE 7-22, Chapters 5 and 6 are unconservative for stiff structural elements of buildings⁵. An alternate impact load formulation is recommended in Equation 3.7-11 for improved safety and more transparent recognition of parameters that influence the magnitude of impact loads. This information can be used to form the basis of future proposed changes to ASCE 7.

⁵ It should be noted, however, that in the case of more flexible building façades and dry floodproofing systems, ASCE 7-22, Chapter 5 and 6 equations likely over-predict impact loads. Flexible components and dry floodproofing systems were not considered as part of the experimental and numerical studies, and have not been evaluated.

4.5 Recommendations for Further Study

Laboratory and numerical experiments considered wave and current flow through a rectangular array of rigid buildings with a consistent size and spacing. Waves and currents were perpendicular to the shoreline and the rows of buildings in the array, and the landward boundary of the array drained into a channel, allowing a net flow of fluid through the array. In most cases, the array was regular, with the buildings aligned and the gaps between buildings (channels) continuous. In limited cases, irregularities were introduced into the array through building offsets occurring between rows.

Even with these simplifying conditions, the experimental setup and numerical computational effort were significant. Although the resulting findings and recommendations are useful, and can be applied directly or extrapolated with judgement to a broad range of conditions, further study is recommended to address conditions that have not yet been investigated.

The following additional studies are suggested to support practical application of the results to additional cases for design practice, or to more comprehensively develop future code change proposals related to flood design requirements in building codes and standards:

- **Oblique Waves and Currents.** Waves and currents approaching an array at an oblique angle are expected to result in additional alongshore flow that will change the wave, current, and debris impact conditions throughout the array. Study of oblique waves and currents is needed to expand application to cases where waves approach the shoreline and built environment at angles up to approximately 20 degrees from the shore-perpendicular direction.
- **Irregular Arrays.** Geometric variations, including building offsets and the size and spacing of buildings in both the cross-shore and alongshore directions, are expected to influence propagation of waves, currents, and debris through an array, and alter the wave and debris sheltering provided by seaward rows of buildings in the array. Study of geometric variations in irregular arrays is needed to better capture building size and spacing effects and to expand application to more cases of building offsets occurring within the built environment.
- **Debris Impact Loads on Flexible Elements.** The magnitude of impact loads depends on the flexibility of the debris object and the building element being impacted. The present study was limited to stiff elements. Many building façades and dry-floodproofing systems consist of more flexible elements, and their responses to debris impacts are expected to differ significantly from results for stiff elements. Study of debris impact

on flexible elements is necessary to understand debris impacts on other common building elements.

- **Debris Impact Probabilities.** Debris impact probabilities are expected to vary for different types of debris and with variations in the building array. Study of debris impact probabilities for varying (i.e., regular and irregular) arrays is recommended to determine if different areas of a building (e.g., face, corner, side) should be subject to different criteria for impact loads (similar to wind pressure increases at corners).
- **Debris Damming.** Debris damming has the potential to significantly increase hydrodynamic loading. Study of the potential for debris damming, considering different variations in the building array, is recommended to determine if there are cases in the built environment that warrant more (or less) consideration of the potential for debris damming.
- **Downstream Boundary Conditions.** Boundary conditions at the landward end of the building array can affect the propagation of waves, currents, and debris through the array. Study of alternative boundary conditions, particularly cases where there is no net flow through the array, is necessary to confirm application to other common conditions in the built environment (e.g., ground sloping upward from the shoreline or regions backed by a bluff).

Appendix A

National Academy of Sciences Formula

Coastal development often consists of a number of streets parallel to the shoreline with buildings on each side of the streets. This leads to the idealized case of a number of parallel rows of buildings separated by a fixed distance in both the cross-shore and alongshore directions.

During a coastal storm, storm surge allows waves to attack buildings. The first row of buildings will feel the full force of the incident waves, but subsequent rows are partially sheltered by the seaward rows. The National Academy of Sciences (NAS) *Methodology for Calculating Wave Action Effects Associated with Storm Surges* (NAS, 1977) uses wave energy to determine the transmission of waves passing through rows of buildings.

From the geometry of the building array, a gap ratio, r , is defined as the percentage of the shorefront represented by gaps between the buildings. The ratio, r , can be computed from the sum of the gaps between buildings divided by the alongshore length of the building array, and is a number less than 1. The number $(1 - r)$ is then the percentage of the shorefront that is blocked by buildings.

From linear wave theory, the amount of energy per unit length of shorefront is $E = 1/8\rho g H_i^2$, where ρ is the density of water, g is the acceleration of gravity, and H_i is the incident wave height.

The wave energy striking a row of buildings is partially transmitted through the gaps between the buildings and reflected or dissipated at the buildings. The relative energy is the energy at the face of a given row, divided by the energy arriving at the first row of buildings. If the transmission of the wave energy is examined through a 10-row building array, the wave energy impinging on the second row of buildings is r times the wave energy impacting the first row, and the third row would have r^2 times the energy of the first row. The relative energy on the front (seaward) face of buildings in each row is shown in Table A.1-1.

Table A.1-1 Wave Energy Transmission Through a Building Array as a Function of Rows and r

| Row Number | 1 | 2 | 3 | 4 | 5 | 6 | 7 | 8 | 9 | 10 |
|---|-----------|-------------|-------------|-------------|-------------|-------------|-------------|-------------|-------------|-----------|
| Relative Energy on Front Face | 1.0 | r | r^2 | r^3 | r^4 | r^5 | r^6 | r^7 | r^8 | r^9 |
| Number of Seaward Rows, n | 0 | 1 | 2 | 3 | 4 | 5 | 6 | 7 | 8 | 9 |
| Reflected Energy on Back Face | $(1-r) r$ | $(1-r) r^2$ | $(1-r) r^3$ | $(1-r) r^4$ | $(1-r) r^5$ | $(1-r) r^6$ | $(1-r) r^7$ | $(1-r) r^8$ | $(1-r) r^9$ | 0 |

Note: In this table, n is the number of seaward rows of buildings providing shelter.

To convert wave energy to wave height for each row, the square root of the relative wave energy is used (i.e., the square root of the entries in the second row of Table A.1-1). The square root of relative wave energy is then multiplied by the incident wave height, H_i , yielding the NAS formula for wave height at row ($n + 1$):

$$H_{(n+1)} = r^{n/2} H_i \quad (\text{A.1-1})$$

where n is the number of seaward rows of buildings providing shelter to the row under consideration.

The wave energy striking a row of buildings is partially reflected, with a maximum value of $(1 - r)$ times the energy arriving at that row. This energy then impinges on the back (landward) face of the row of buildings immediately seaward of the row. For the landward face of row 1 buildings, the relative wave energy reflected from row 2 is $(1 - r) r$. In all subsequent rows (except the back row), the reflected energy on the back face of a building is $(1 - r) r$ times the energy on the front face of the building in the row under consideration.

The relative reflected energy on the back (landward) face of a building due to reflection from the next landward row of buildings is also shown in Table A.1-1. The reflected wave height on the landward face of a row of buildings, $H_{R,n}$, is then the square root of the reflected wave energy multiplied by the incident wave height:

$$H_{R,n} = (1 - r)^{1/2} r^{n/2} H_i \quad (\text{A.1-2})$$

where n is the number of rows of buildings seaward of the reflecting row.

The reflected wave from the next landward row of buildings is likely to be the largest wave striking the landward face of a building, but there are

additional (smaller) waves that are reflected back from other more landward rows of buildings. For example, in row 1, the waves impinging on the landward face of the building have been reflected from each of the 9 landward rows. In row 1 ($n = 0$), the relative energy reflected from row 2 is $(1 - r)r$. But row 2 buildings were also exposed to reflected wave energy of $(1 - r)r^2$ from row 3, a portion of which (r) is transmitted seaward through the gaps in row 2 to impact row 1. In terms of relative energy, E_R , for three rows of buildings, the landward face of the first row of buildings is exposed to reflections from the second and third rows:

$$E_{R,n=0} = (1 - r)r + (1 - r)r^2 \cdot r = (1 - r)r + (1 - r)r^3 \quad (\text{A.1-3})$$

For ten rows, the reflected wave energy hitting the landward face of the first row, due to reflections from all the landward rows, is:

$$E_{R,n=0} = \sum_{n=1}^9 (1 - r)r^{2n-1} \quad (\text{A.1-4})$$

In a similar fashion, the sum of reflected waves at any row can be determined. However, it would not be correct to take the square root of the above equation to determine the total reflected wave height on the back (landward) face of row 1. This is because the reflected waves from subsequent rows will likely not be in phase as they arrive at the back face of row 1 buildings, as they will arrive at different times, sometimes adding, and sometimes cancelling other reflected waves. In the event that the reflected waves were all in phase (as occurs in Bragg scattering when there is a specific spacing between rows), then they would superimpose to be about as large as the incident wave, but such an event is highly unlikely and is not considered further here.

This analysis considers only the primary reflection from each landward row. But the number of reflections is much larger, as waves reflect from a landward row, reflect again from a seaward row, and then reflect again from a landward row, and so on. It is assumed that each reflected wave accumulates a $(1 - r)$ multiplier for each reflection, and an r multiplier for each transmission through a row, making each subsequent wave smaller than before. Multiple reflections (at different phases) would not be expected to result in wave energies larger than those given in Table A.1-1, and multiple reflections are not recommended for consideration in design.

Figure A.1-1 shows the maximum wave height on the landward face of a row of buildings under the following assumptions: (1) full reformation of waves beyond the sheltering rows; (2) zero energy dissipation; (3) 100% wave

reflection; and (4) consideration of only the primary reflection from each landward row.

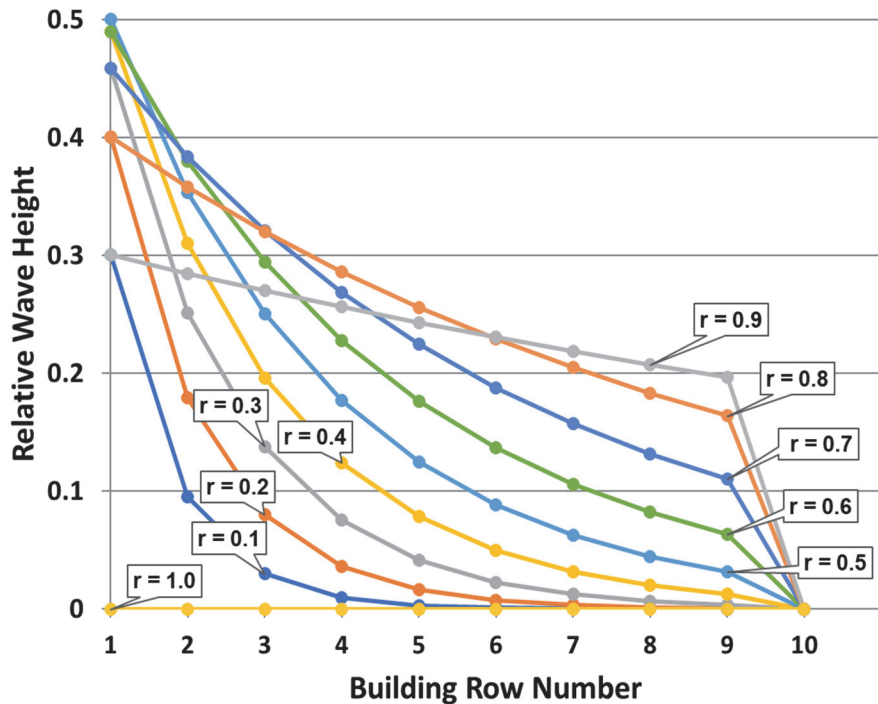


Figure A.1-1 Relative wave height, H/H_i , for reflected waves on the landward face of a building in a given row, as a function of gap ratio, r . The reflected wave is from the next landward row.

In the figure, it can be seen that the largest relative wave heights occur on the back (landward) face of row 1, and the maximum value of approximately 0.5 occurs with gap ratios of $r = 0.4, 0.5, and 0.6 . Because wave loads are proportional to the square of wave height, squaring the values in Figure A.1-1 would yield approximate values for relative wave loads. Based on the assumptions used to develop the plot, the maximum reflected wave load would be 0.25 times the incident wave load and would occur on the back face of row 1. In all subsequent rows, relative wave heights are less than approximately 0.3 for most values of r , which, when squared, would indicate that reflected wave load on the back face of subsequent rows is less than 10% of the incident wave load on row 1.$

In this derivation, it is assumed that waves transmitting past a row of buildings reform into a uniform wave crest before striking the next row (i.e., diffraction of the waves is considered to be perfect), and all energy dissipation mechanisms have been neglected. In actuality, buildings in closely spaced rows will be shadowed from some of the wave action, and contact with the buildings and shoreline will result in energy dissipation. It is

almost certain that there will be less than full reflection due to some level of energy dissipation, so the waves calculated herein are the theoretical maximum reflected waves.

Symbols

| | |
|--------------------|--|
| A | frontal area of a structure subject to drag force |
| B | wave height transmission coefficient |
| b | horizontal width of structures |
| C_B | ASCE 7-22 blockage coefficient |
| C_D | drag coefficient; also ASCE 7-22 depth coefficient |
| C_I | ASCE 7-22 importance factor |
| C_O | ASCE 7-22 orientation factor; also drag coefficient |
| $C_{R,\max}$ | modification to ASCE 7-22 dynamic response coefficient |
| CR | collision ratio for debris impacts |
| C_s | factor to account for higher mode effects; also ASCE 7-22 velocity stagnation coefficient for debris impacts |
| d | cross-shore distance between rows of structures in an array |
| d^* | dimensionless ratio of cross-shore distance between rows, d , divided by structure width, b |
| F | ASCE 7-22 dynamic debris load to structure |
| $F_{D,\max}$ | maximum drag force |
| F_i | ASCE 7-22 instantaneous debris impact force |
| F_{ni} | ASCE 7-22 peak debris load |
| $F_{n,\max}$ | maximum load with n sheltering rows |
| $F_{n,\max}^{(0)}$ | maximum load for structure when all n sheltering rows are removed |
| $F_{0,\max}$ | maximum load with 0 sheltering rows |

| | |
|-----------------------|---|
| $F_{r,x,\max}$ | synthesized prediction of maximum debris loads in x-direction |
| $F_{r,y,\max}$ | synthesized prediction of maximum debris loads in y-direction |
| F_x | structural load in the cross-shore direction |
| F_y | structural load in the alongshore direction |
| | |
| h | stillwater depth |
| H | solitary wave height |
| H_i | incident wave height |
| H_s | significant wave height |
| H_t | transmitted wave height |
| | |
| $I_{0,x}$ | impulse transmitted to structure in the x-direction |
| $I_{0,y}$ | impulse transmitted to structure in the y-direction |
| $\bar{I}_{0,x}^{2nd}$ | second largest dimensionless impulse in the x-direction from laboratory tests |
| $\bar{I}_{0,x}$ | dimensionless debris impulse in the x-direction |
| $\bar{I}_{0,y}$ | dimensionless debris impulse in the y-direction |
| I_{tsu} | ASCE 7-22 importance coefficient |
| | |
| LRF | load reduction factor |
| $LRFA_n$ | load reduction factor A for n rows of shelter |
| $LRFB_n$ | load reduction factor B for n rows of shelter |
| $LRFC_n$ | load reduction factor C for n rows of shelter |
| | |
| m | debris mass |
| $M_{BE,\max}$ | maximum bare earth momentum flux |
| MRF | momentum flux reduction factor |
| | |
| n | row number; also number of seaward rows providing shelter |
| $N_{\text{row } n}$ | number of debris collision events in a row |

| | |
|---------------|---|
| N_T | total number of debris events |
| o | alongshore offset between centerlines of structures in adjacent rows in an array |
| o^* | dimensionless ratio of alongshore offset divided by half of the alongshore center-to-center spacing of structures in an array |
| P_i | probability of load exceedance for i^{th} largest measured load |
| p_n | representative wave-current-debris impulse |
| Q | volumetric flow rate |
| r | NAS open gap ratio, equal to the alongshore gap between structures divided by the alongshore center-to-center spacing of structures in an array |
| R_i | magnitude of i^{th} largest measured load |
| R_{\max} | ASCE 7-22 dynamic response coefficient for debris impacts |
| RRF | runup reduction factor |
| S_f | scale factor for error function wave generation. |
| t | time |
| T_n | natural period of structural system |
| $T_{n,x}$ | period of n^{th} structural mode in x-direction |
| $T_{n,y}$ | period of n^{th} structural mode in y-direction |
| T_p | peak wave period |
| u | horizontal fluid velocity |
| $u_{BE,\max}$ | maximum bare earth horizontal fluid velocity at a location |
| $u_{n,\max}$ | maximum horizontal fluid velocity with n rows of shelter |

| | |
|------------------|--|
| V_b | ASCE 7-22 debris velocity |
| VRF | velocity reduction factor |
| w^* | relative structural blockage ratio |
| W | ASCE 7-22 debris weight |
| x | cross-shore coordinate |
| y | alongshore coordinate |
| $\delta(t)$ | Dirac delta function |
| Δt | debris impact duration |
| η | water surface elevation |
| $\eta_{BE,\max}$ | maximum bare earth water surface elevation at a location |
| $\eta_{n,\max}$ | maximum water surface elevation with n rows shelter |
| λ | dynamic loading response function |
| ξ | structural damping ratio |
| ω_d | damped radial frequency of structural system for mode n |
| ω_n | natural radial frequency of structural system for mode n |

References

ASCE, 2014, *Flood Resistant Design and Construction*, ASCE/SEI Standard 24-14, American Society of Civil Engineers, Reston Virginia.

ASCE, 2022, *Minimum Design Loads and Associated Criteria for Buildings and Other Structures*, ASCE/SEI Standard 7-22, American Society of Civil Engineers, Reston Virginia.

FEMA, 1981, *User's Manual for Wave Height Analysis to Accompany the Methodology for Calculating Wave Action Effects Associated with Storm Surges (National Academy of Sciences, 1977)*, Federal Emergency Management Agency, Washington, D.C.

FEMA, 2011, *Coastal Construction Manual, Principles and Practices of Planning, Siting, Designing, Constructing, and Maintaining Residential Buildings in Coastal Areas (Fourth Edition)*, FEMA P-55, Federal Emergency Management Agency, Washington, D.C.

Higuera, P., Lara, J.L., Losada, I.J., 2013, “Realistic wave generation and active wave absorption for Navier-Stokes models: Application to openFOAM®,” *Journal of Coastal Engineering*, Vol. 71, pp. 102-118.

Moon, W.C., Chiew, L.Q., Cheong, K.W., Tee, Y.C., Chun, J.B., Lau, T.L., 2019, “An experimental study for estimating tsunami wave forces acting on building with seaward and landward macroroughness,” *Ocean Engineering*, Vol. 186, 106116.

Moris, J.P., 2022, *Wave and Debris Loading in Developed Coastal Regions*, Ph.D. Dissertation, University of Notre Dame, Notre Dame, Indiana.

Moris, J.P., Burke, O., Kennedy, A.B., and Westerink, J.J., 2022, “Wave-current impulsive debris loading on a coastal building array,” *Journal of Waterway, Port, Coastal, and Ocean Engineering*, under review.

Moris, J.P., Kennedy, A.B., and Westerink, J.J., 2021, “Tsunami wave run-up load reduction inside a building array,” *Journal of Coastal Engineering*, Vol. 169, <https://doi.org/10.1016/j.coastaleng.2021.103910>.

NAS, 1977, *Methodology for Calculating Wave Action Effects Associated with Storm Surges*, National Research Council, Panel on Wave Action Effects Associated with Storm Surges, National Academy of Sciences, Washington, D.C.

Park, H., Cox, D.T., Shin, S., 2019, “Physical modeling of horizontal and vertical tsunami forces on the elevated overland structure,” *Journal of Coastal Research*, Vol. 91, pp. 51-55.

Sogut, E., Sogut, D.V., Farhadzadeh, A., 2019, “Effects of building arrangement on flow and pressure fields generated by a solitary wave interacting with developed coasts,” *Advances in Water Resources*, Vol. 134, 103450.

Tomiczek, T., Prasetyo, A., Mori, N., Yasuda, T., and Kennedy, A., 2016, “Physical modelling of tsunami onshore propagation, peak pressures, and shielding effects in an urban building array,” *Coastal Engineering*, Vol. 117, pp. 97-112.

Yang, W., Wen, Z., Li, F., Li, Q., 2018, “Study on tsunami force mitigation of the rear house protected by the front house,” *Journal of Ocean Engineering and Science*, Vol. 159, pp. 268-279.

Yeh, H., 2006, “Maximum fluid forces in the tsunami runup zone,” *Journal of Waterway, Port, Coastal, and Ocean Engineering*, Vol. 132, pp. 496-500.

Project Participants

Applied Technology Council

Jon A. Heintz (Project Manager)
Applied Technology Council
201 Redwood Shores Parkway, Suite 240
Redwood City, California 94065

University of Notre Dame

Andrew Kennedy (Principal Investigator)
University of Notre Dame
College of Engineering
168 Fitzpatrick Hall
Notre Dame, Indiana 46556

Project Oversight Committee

Christopher P. Jones
(Project Technical Director)
5525 Jomali Drive
Durham, NC 27705

A. Christopher Cerino
STV Inc.
225 Park Ave South
New York, New York 10003

Robert A. Dalrymple
Northwestern University
Dept. of Civil and Environmental Engineering
2145 Sheridan Road, A222
Evanston, Illinois 60208

Seth Thomas
KPFF
111 SW Fifth Avenue, Suite 2600
Portland, Oregon 97204

Working Group Members

Joaquin P. Moris
University of Notre Dame
College of Engineering
168 Fitzpatrick Hall
Notre Dame, Indiana 46556

Applied Technology Council Directors

ATC Board of Directors (1973-Present)

| | | | |
|--------------------------|--------------------|--------------------------|--------------------|
| Milton A. Abel | (1979-1985) | Melvyn Green | (2001-2002) |
| Dan Allwardt | (2010-2013) | Lawrence G. Griffis* | (2002-2008) |
| James A. Amundson* | (2010-2016) | Kurtis R. Gurley | (2011-2018) |
| James C. Anderson | (1978-1981) | Gerald H. Haines | (1981-82, 1984-85) |
| Victoria Arbitrio* | (2011-2018) | William J. Hall | (1985-1986) |
| Thomas G. Atkinson* | (1988-1994) | Ronald O. Hamburger | (1999-2000) |
| Steven M. Baldridge | (2000-2003) | Robert W. Hamilton | (2002-2005) |
| Albert J. Blaylock | (1976-1977) | James R. Harris* | (2004-2010) |
| David C. Breiholz | (2004-2006) | Gary C. Hart | (1975-1978) |
| Melissa Burton | (2019-2025) | Erleen Hatfield | (2011-2017) |
| Patrick Buscovich* | (2000-2009) | Robert H. Hendershot | (2000-2001) |
| James R. Cagley* | (1998-2004) | Lyman Henry | (1973) |
| H. Patrick Campbell | (1989-1990) | Richard L. Hess | (2000-2003) |
| Lyle P. Carden | (2018-2024) | James A. Hill | (1992-95, 2003-04) |
| Arthur N. L. Chiu* | (1996-2002) | Ernest C. Hillman, Jr. | (1973-1974) |
| Anil Chopra | (1973-1974) | Eve Hinman | (2002-2008) |
| Richard Christopherson* | (1976-1980) | Ephraim G. Hirsch | (1983-1984) |
| Lee H. Cliff | (1973) | Douglas C. Hohbach* | (2015-2021) |
| Kelly Cobeen | (2021-2024) | William T. Holmes* | (1983-1987) |
| Leighton Cochran | (2011-2017) | Warner Howe | (1977-1980) |
| Michael L. Cochran | (2018-2024) | Edwin T. Huston* | (1990-1997) |
| John M. Coil* | (1986-87, 1991-97) | David Hutchinson | (2004-2010) |
| Eugene E. Cole | (1985-1986) | Jeremy Isenberg | (2002-2005) |
| Anthony B. Court | (2001-04, 2016-22) | Paul C. Jennings | (1973-1975) |
| Edwin T. Dean* | (1996-2002) | Carl B. Johnson | (1974-1976) |
| Robert G. Dean | (1996-2001) | Carrie J. Johnson* | (2017-2023) |
| Gregory G. Deierlein | (2003-2009) | Edwin H. Johnson | (1988-89, 1998-01) |
| James M. Delahay* | (1999-2005) | Stephen E. Johnston* | (1973-75, 1979-80) |
| Edward F. Diekmann | (1978-1981) | Christopher P. Jones* | (2001-2008) |
| Burke A. Draheim | (1973-1974) | Joseph Kallaby* | (1973-1975) |
| John E. Droege | (1973) | Donald R. Kay | (1989-1992) |
| Donald O. Dusenberry* | (2018-2024) | T. Robert Kealey* | (1984-1988) |
| Michael D. Engelhardt* | (2014-2020) | H. S. (Pete) Kellam | (1975-1976) |
| David A. Fanella | (2010-2011) | Andrew B. Kennedy | (2013-2019) |
| Nicholas F. Forell* | (1989-1996) | Ryan A. Kersting* | (2017-2023) |
| Douglas A. Foutch | (1993-1997) | Helmut Krawinkler | (1979-1982) |
| Paul Fratessa | (1991-1992) | Steven Kuan | (2006-2009) |
| Sigmund A. Freeman | (1986-1989) | James S. Lai | (1982-1985) |
| Maria E. Moreyra Garlock | (2020-2023) | Mark H. Larsen | (2003-2006) |
| Nancy L. Gavlin* | (2011-2016) | Gerald D. Lehmer | (1973-1974) |
| Ramon Gilsanz* | (2005-2012) | Roberto T. Leon* | (2012-2018) |
| Barry J. Goodno | (1986-1989) | Christopher W. Letchford | (2017-2023) |
| Mark R. Gorman | (1984-1987) | Marc L. Levitan | (2006-2010) |

| | | | |
|------------------------|--------------------|-------------------------|--------------------|
| James R. Libby | (1994-1998) | John M. Roberts | (1973) |
| Charles Lindbergh | (1989-1992) | James Robinson | (2005-2008) |
| R. Bruce Lindermann | (1983-1986) | Charles Roeder | (1997-00, 2009-12) |
| Bret Lizundia* | (2009-2015) | Spencer Rogers | (2007-2013) |
| L. W. Lu | (1987-1990) | Arthur E. Ross* | (1985-91, 1993-94) |
| Walter B. Lum | (1975-1978) | C. Mark Saunders* | (1993-2000) |
| Kenneth A. Luttrell | (1991-1999) | Walter D. Saunders* | (1975-1979) |
| James O. Malley* | (2016-2022) | Wilbur C. Schoeller | (1990-1991) |
| Newland J. Malmquist | (1997-2000) | Samuel Schultz* | (1980-1984) |
| Melvyn H. Mark | (1979-1982) | Donald R. Scott* | (2009-2015) |
| John A. Martin | (1978-1982) | Lawrence G. Selna | (1981-1984) |
| Stephen McReavy | (1973) | Daniel Shapiro* | (1977-1981) |
| John F. Meehan* | (1973-1978) | Joseph B. Shepard | (2008-2014) |
| Andrew T. Merovich* | (1996-2003) | Jonathan G. Shipp | (1996-2000) |
| David L. Messinger | (1980-1983) | Howard Simpson* | (1980-1984) |
| Bijan Mohraz | (1991-1997) | Robert Smilowitz | (2008-2011) |
| William W. Moore* | (1973-1976) | Thomas L. Smith | (2008-2014) |
| Manuel Morden | (2006-2012) | Mete Sozen | (1990-1993) |
| Ugo Morelli | (2004-2006) | William Staehlin | (2002-03, 2013-19) |
| Gary Morrison | (1973) | Scott Stedman | (1996-1997) |
| Robert Morrison | (1981-1984) | Donald R. Strand | (1982-1983) |
| Ronald F. Nelson | (1994-1995) | James L. Stratta | (1975-1979) |
| Joseph P. Nicoletti* | (1975-1979) | Edward J. Teal | (1976-1979) |
| Sissy Nikolauou | (2017-2020) | W. Martin Tellegen | (1973) |
| Bruce C. Olsen* | (1978-1982) | John C. Theiss* | (1991-1998) |
| Gerard Pardoen | (1987-1991) | Seth Thomas | (2022-2025) |
| Robert B. Paullus, Jr. | (2014-2017) | Charles H. Thornton* | (1992-00, 2005-11) |
| Stephen H. Pelham* | (1998-2005) | James L. Tipton | (1973) |
| Norman D. Perkins | (1973-1976) | Christos Tokas | (2019-2025) |
| Richard J. Phillips | (1997-2000) | Ivan Viest | (1975-1977) |
| Maryann T. Phipps | (1995-96, 1999-02) | Ajit S. Virdee* | (1977-80, 1981-85) |
| Sherrill Pitkin | (1984-1987) | J. John Walsh | (1987-1990) |
| Chris D. Poland | (1984-1987) | Williston L. Warren, IV | (2012-2018) |
| Edward V. Pollack | (1973) | Robert S. White | (1990-1991) |
| Egor P. Popov | (1976-1979) | James A. Willis* | (1980-81, 1982-86) |
| Robert F. Preece* | (1987-1993) | Thomas D. Wosser | (1974-1977) |
| David O. Prevatt | (2018-2023) | Loring A. Wyllie | (1987-1988) |
| H. John Price* | (2004-2011) | Kent Yu | (2015-2018) |
| Ahmad Rahimian | (2021-2023) | Edwin G. Zacher | (1981-1984) |
| Lawrence D. Reaveley* | (1985-91, 2000-03) | Theodore C. Zsutty | (1982-1985) |
| Jose Restrepo | (2022-2025) | *ATC President | |
| Philip J. Richter* | (1986-1989) | | |

ATC Executive Directors (1973-Present)

| | | | |
|---------------|----------------|--------------------|-------------|
| Jon A. Heintz | (2015-present) | Christopher Rojahn | (1981-2015) |
| Ronald Mayes | (1979-1981) | Roland L. Sharpe | (1973-1979) |

Applied Technology Council

ATC Sponsors, Supporters, and Contributors

Sponsors

James R. and Sharon K. Cagley
Rutherford & Chekene
John M. Coil
Computers & Structures, Inc.
Degenkolb Engineers
Gilsanz Murray Steficek
Sang Whan Han
Edwin T. Huston
KPFF Consulting Engineers
Nabih Youssef & Associates
Robert B. Paullus
Rojahn-King Family
Structural Engineers Association of California
Charles H. Thornton
Walter P. Moore & Associates

Supporters

Erleen Hatfield
Contributors
Omar D. Cardona
Lawrence D. Reaveley
John C. Theiss

ATC Projects and Report Information

ATC conducts applied research and technology transfer projects for which a consensus of engineering opinion is necessary or beneficial. ATC's primary audience includes engineering design professionals, federal, state, and local government entities, and other stakeholders in the global hazard mitigation community. In its nearly 50-year history, ATC has conducted more than 150 projects and published more than 300 major reports and publications.

ATC reports have identified and encouraged needed structural engineering research at the national level, contributed to the development and evolution of building codes and standards, and served to define seismic and other engineering design practice in the United States and the world. Because ATC products are consensus-based and non-proprietary, they are immediately accepted by the profession and hold lasting value to engineering practitioners. Although technology continues to evolve, many older reports remain useful as a historical reference or as a guide for current engineering practice.

A complete listing of ATC Projects and Report Information is available at www.ATCouncil.org.